9-1-2013

Gas Lines from the 5-Myr old Optically Thin Disk around HD141569A

W F. Thi
Institut de Planetologie et d'Astrophysique

C Pinte
Institut de Planetologie et d'Astrophysique

E Pantin
Universite Paris Diderot

J C. Augereau
Institut de Planetologie et d'Astrophysique

G Meeus
UAM Campus Cantoblanco

See next page for additional authors

Recommended Citation

Please use publisher's recommended citation.

Authors
W F. Thi, C Pinte, E Pantin, J C. Augereau, G Meeus, F Menard, C Martin-Zaidi, P Woitke, P Riviere-Marichalar, I Kamp, A Carmona, G Sandell, C Eiroa, W Dent, B Montesinos, G Aresu, R Meijerink, M Spaans, G White, D Ardila, J Lebreton, I Mendigutia, and Sean D. Brittain

Astronomy & Astrophysics manuscript no. hd141569_herschel
September 23, 2013

arXiv:1309.5098v1 [astro-ph.GA] 19 Sep 2013

Gas lines from the 5-Myr old optically thin disk around HD141569A[⋆]

Herschel observations and modeling [⋆⋆]

W.-F. Thi[1], C. Pinte[1], E. Pantin[2], J.C. Augereau[1], G. Meeus[3], F. Ménard[1, 4], C. Martin-Zaïdi[1], P. Woitke[5], P. Riviere-Marichalar[6] I. Kamp[6], A. Carmona[1], G. Sandell[7], C. Eiroa[3], W. Dent[8], B. Montesinos[3], G. Aresu[6], R. Meijerink[6], M. Spaans[6], G. White[9, 10], D. Ardila[11], J. Lebreton[1], I. Mendigutía[12], S. Brittain[12]

[1] UJF-Grenoble 1 / CNRS-INSU, Institut de Planétologie et d'Astrophysique (IPAG) UMR 5274, Grenoble, F-38041, France
e-mail: `Wing-Fai.Thi@obs.ujf-grenoble.fr`
[2] Laboratoire AIM, CEA/DSM - CNRS - Université Paris Diderot, IRFU/SAP, F-91191 sur Yvette, France
[3] Dep. de Física Teórica, Fac. de Ciencias, UAM Campus Cantoblanco, 28049 Madrid, Spain
[4] UMI – LFCA, CNRS / INSU France, and Dept. de Astronomia y Obs. Astronomico Nacional, Universidad de Chile, Casilla 36-D, Correo Central, Santiago, Chile (UMI 3386)
[5] SUPA, School of Physics & Astronomy, University of St. Andrews, North Haugh, St. Andrews KY16 9SS, UK
[6] Kapteyn Astronomical Institute, P.O. Box 800, 9700 AV Groningen, The Netherlands
[7] SOFIA-USRA, NASA Ames Research Center, Mail Stop N211-3, Building N211/Rm. 249, Moffett Field, CA 94035, USA
[8] ALMA, Avda Apoquindo 3846, Piso 19, Edificio Alsacia, Las Condes, Santiago, Chile
[9] Astrophysics Group, Department of Physics & Astronomy, The Open University, UK
[10] RAL Space, The Rutherford Appleton Laboratory, Didcot, Oxfordshire, UK
[11] NASA Herschel Science Center, California Institute of Technology, Mail Code 100-22, Pasadena, CA 91125, USA
[12] Department of Physics and Astronomy, 118 Kinard Laboratory, Clemson University, Clemson, SC 29634, USA

Received 2013; accepted 10 september 2013

ABSTRACT

Context. The gas- and dust dissipation processes in disks around young stars remain uncertain despite numerous studies. At the distance of ~ 99–116 pc, HD141569A is one of the nearest HerbigAe stars that is surrounded by a tenuous disk, probably in transition between a massive primordial disk and a debris disk. Atomic and molecular gases haves been found in the structured 5-Myr old HD141569A disk, making HD141569A the perfect object within which to directly study the gaseous atomic and molecular component.
Aims. We wish to constrain the gas and dust mass in the disk around HD141569A.
Methods. We observed the fine-structure lines of O I at 63 and 145 μm and the C II line at 157 μm with the *PACS* instrument onboard the *Herschel Space Telescope* as part of the open-time large programme GASPS. We complemented the atomic line observations with archival *Spitzer* spectroscopic and photometric continuum data, a ground-based *VLT-VISIR* image at 8.6 μm, and ^{12}CO fundamental ro-vibrational and pure rotational J=3–2 observations. We simultaneously modeled the continuum emission and the line fluxes with the Monte Carlo radiative transfer code MCFOST and the thermo-chemical code ProDiMo to derive the disk gas- and dust properties assuming no dust settling.
Results. The models suggest that the oxygen lines are emitted from the inner disk around HD141569A, whereas the [C II] line emission is more extended. The CO submillimeter flux is emitted mostly by the outer disk. Simultaneous modeling of the photometric and line data using a realistic disk structure suggests a dust mass derived from grains with a radius smaller than 1 mm of ~ 2.1×10^{-7} $M_\odot$ and from grains with a radius of up to 1 cm of 4.9×10^{-6} $M_\odot$. We constrained the polycyclic aromatic hydrocarbons (PAH) mass to be between 2×10^{-11} and 1.4×10^{-10} $M_\odot$ assuming circumcircumcoronene ($C_{150}H_{30}$) as the representative PAH. The associated PAH abundance relative to hydrogen is lower than those found in the interstellar medium (3×10^{-7}) by two to three orders of magnitude. The disk around HD141569A is less massive in gas (2.5 to 4.9×10^{-4} $M_\odot$ or 67 to 164 $M_\oplus$) and has a flat opening angle (< 10%).
Conclusions. We constrained simultaneously the silicate dust grain, PAH, and gas mass in a ~5-Myr old Herbig Ae disk. The disk-averaged gas-to-dust-mass is most likely around 100, which is the assumed value at the disk formation despite the uncertainties due to disagreements between the different gas tracers. If the disk was originally massive, the gas and the dust would have dissipated at the same rate.

Key words. stars: pre-main-sequence, astrochemistry, protoplanetary disk

1. Introduction

Constraining the gas- and dust mass in the disks around young stars is paramount for our understanding of the planet formation process (e.g., Armitage 2010). The determination of the

---

[⋆] Based on observations made with ESO Telescopes at the La Silla Paranal Observatory under programme ID 079.C-0602(A)

[⋆⋆] Herschel is an ESA space observatory with science instruments provided by Principal Investigator consortia. It is open for proposals for observing time from the worldwide astronomical community.

dust mass can be routinely made by fitting the spectral energy distribution (SED) and images of disks. Sophisticated and reliable radiative-transfer codes are available (e.g., Pinte et al. 2006, 2009; Min et al. 2009; Dullemond & Dominik 2004). The accuracy of the dust mass estimates is limited by the uncertainties in the opacities due to our limited knowledge of the grain composition, the shape, and the size distribution. However, up to now, the estimates of the solid mass in disks are much more accurate than gas-mass estimates, so that most studies assume the interstellar gas-to-dust-mass ratio of 100 remains constant throughout the disk lifetime. The most common method involves the observation of rotational emission lines from CO and its isotopologues ^{13}CO and C^{18}O. The premise of this method is that the typical H_2/CO conversion factor for dense clouds, $\sim 10^{-4}$ for ^{12}CO, remains valid for protoplanetary disks. Most disk gas-mass estimates using this method show that the gas-to-dust ratios in disks may be lower than 100. The reasons for the small disk-gas masses are thought to be CO freeze-out on grain surfaces and/or CO photodissociation, especially for disks with masses lower than 10^{-3} $M_\odot$.

The PACS instrument (Poglitsch et al. 2010) onboard the Herschel Space Telescope (Pilbratt et al. 2010) is sensitive enough to observe lines from species that result from the photodissociation of CO (atomic oxygen and singly ionized carbon) in disks. We used observations of the O and C^+ fine-structure emissions in addition to CO and, when available, ^{13}CO data to constrain accurately the gas mass around the classical T Tauri stars TW Hya (Thi et al. 2010) and ET Cha (Woitke et al. 2011), as well as around the HerbigAe star HD 169142 (Meeus et al. 2010) and HD 163296 (Tilling et al. 2012). These studies are part of the large open-time program *GASPS* (Dent et al. 2013; Mathews et al. 2010; Pinte et al. 2010). The disk gas-to-dust-mass ratio may vary by orders of magnitudes between objects. The gas disk around TW Hya is ten times less massive than the total amount of solids up to 10 cm in radius than in the interstellar medium where the maximum radius is below one micron while the gas remains 100 times more massive in the disk around HD 169142, and over 1000 times more massive in the disk around ET Cha.

In this paper, we extend our study of disk dust and gas masses to the low-mass optically thin disk around HD141569A as a part of the Herschel-GASPS programme. The use of atomic and molecular lines as gas mass tracers has been explored by Kamp et al. (2010).

At a distance of ∼ 99 pc (van den Ancker et al. 1997) to 116.1±8.1 (Merín et al. 2004), HD141569A is one the nearest HerbigAe stars and has an estimated age of 4.7 ± 0.3 Myr (Merín et al. 2004). HD141569A lies at the edge of the high Galactic latitude core MBM37 (Caillault et al. 1995). The disk around HD141569A was first detected from its excess emission over the photospheric flux in the mid-infrared data taken by the *Infrared Astronomical Satellite (IRAS)* (Andrillat et al. 1990; Walker & Wolstencroft 1988; Sylvester et al. 1996). Subsequent high-resolution scattered-light imagings with the *Hubble Space Telescope* showed that HD141569A is surrounded by a complex ring structure with a non-monotonic decreasing surface brightness with radius, instead of a uniformly disk (Augereau et al. 1999; Weinberger et al. 1999). Further coronographic high-quality observations revealed a strong brightness asymmetry interpreted as the signature of a massive planet embedded within the disk (Mouillet et al. 2001; Boccaletti et al. 2003; Wyatt 2005) and two spiral arms that may be due to the companion star (Clampin et al. 2003). The observations constrain the inner ring peak emission at ∼200 ± 5 AU and a width of ∼50 AU. Direct and coronographic imaging studies at optical and near-infrared wavelengths are not sensitive to material within 100 AU. Ground-based mid-infrared imagings at 10.8 and 18.2 μm (Fisher et al. 2000) and at 17.9 and 20.8 μm (Marsh et al. 2002) support the presence of warm dust grains within 100 AU to the star, as predicted by Augereau et al. (1999) to explain the mid-infrared spectral energy distribution. Fits to the SED enable the solid disk mass to be estimated as 6.7×10^{-6} $M_\odot$ or 2.2 $M_\oplus$ (Li & Lunine 2003). The fit to the SED also suggests that grains have grown to ∼ 10 cm. PAH emissions have been detected toward HD141569A by the Spitzer Space Telescope (Keller et al. 2008).

Table 1. PACS photometry with 1 σ shot-noise error. Calibration uncertainties are 5% and 10% in the blue, and red filter respectively.

Band	λ (μm)	Flux (Jy)
blue	70	3.09 ± 0.11
red	160	1.33 ± 0.05

HD141569A shows a rich CO ro-vibrational ($v \geq 1$, Δv=1) emission spectrum around 4.65 μm (Brittain et al. 2003; Goto et al. 2006; Brittain et al. 2007; Salyk et al. 2011), testifying of the presence of warm molecular gas. The spatially resolved data showed that CO emission arises from beyond 11 ± 2 AU (Goto et al. 2006). No companion more massive than 22 Jupiter mass at 7 AU has been found by the sparse aperture-masking technique (Lacour et al. 2011).

The fine-structure line emission has been studied by Jonkheid et al. (2006) using a 1+1D chemo-physical code. They made predictions for the [O I] 63 and 145 μm and [C II] 157 μm lines based on a model that matched the ^{12}CO J=3-2 observations by Dent et al. (2005) using the *James Clerk Maxwell Telescope (JCMT)*. Sandell et al. (2011) observed the continuum emission at 450 μm and 850 μm with *SCUBA* at the *JCMT*. In this paper, we use the continuum Monte Carlo code MCFOST to model the continuum photometry and images (Pinte et al. 2006), and the chemo-physical code ProDiMo, which self-consistently computes the chemistry and gas cooling of disks (Woitke et al. 2009; Thi et al. 2011, 2013) to interpret the *Herschel* and *JCMT* line data.

The paper is organized as follows: the *Herschel* data are shown in Sect. 2 where a simple analysis is also provided. In Sect. 2.2, we discuss the possible contribution of interstellar emission to the observed fine-structure fluxes. A modeling of the continuum with MCFOST and the gas lines with ProDiMo is presented in Sect. 3 and 4. The derived solid and gas masses in HD141569A are discussed in Sect. 5, followed by the conclusions in Sect. 6.

2. Herschel and VISIR observations and first analysis

2.1. Observations

For HD141569A we obtained photometry in the blue (70 μm) and red (160 μm) band (obsid 2342215382 and 1342215383) of the PACS camera by assembling mini-scan scan maps with a scan speed of $20''s^{-1}$ and a scan length of $2'$. The total duration of the scan for this map was 731 sec, with an on-source time of 146 seconds. The results of the photometry are given in Table 1 and have an absolute accuracy estimated to be 5% for the blue channel and 10% for the the red channel. These values agree

Table 2. Lines observed by *Herschel-PACS* (Meeus et al. 2012). The errors are 1σ and the upper limits are 3σ. The calibration error adds an extra ~ 30% uncertainty. The CO data are taken from Dent et al. (2005) and have uncertainties of ~ 30%. n. a. means not available.

Line	λ (μm)	Cont. flux (Jy)	Line flux (10^{-18} W m^{-2})
[O I] $^3P_1 \rightarrow ^3P_2$	63.183	2.98 ± 0.01	245.3 ± 4.8
o-H_2O $8_{18} - 7_{07}$	63.324	2.98 ± 0.01	$<$ 8.6
CO J=36 → 35	72.85	3.91 ± 0.03	$<$ 10.6
CO J=33 → 32	76.36	3.30 ± 0.03	$<$ 10.4
p-H_2O $3_{22} - 2_{11}$	89.99	2.89 ± 0.03	$<$ 7.6
CO J=29 → 28	90.16	2.77 ± 0.02	$<$ 5.9
CO J=18 → 17	144.78	1.09 ± 0.07	$<$ 21.5
[O I]$^3P_0 \rightarrow ^3P_1$	145.525	1.29 ± 0.01	24.9 ± 1.4
[C II] $^2P_{3/2} \rightarrow ^2P_{1/2}$	157.74	1.18 ± 0.02	11.4 ± 1.8
o-H_2O $2_{12} - 1_{01}$	179.52	0.85 ± 0.03	$<$ 6.0
o-H_2O $2_{21} - 2_{12}$	180.42	0.82 ± 0.04	$<$ 6.9
SO_2 $27_{11,17} - 26_{10,16}$[a]	189.67	0.50 ± 0.10	5.0 ± 0.7
^{12}CO J=3–2	866.96	n. a.	0.1 ± 0.008

[a] Tentative detection and assignment. The line is probably an artifact.

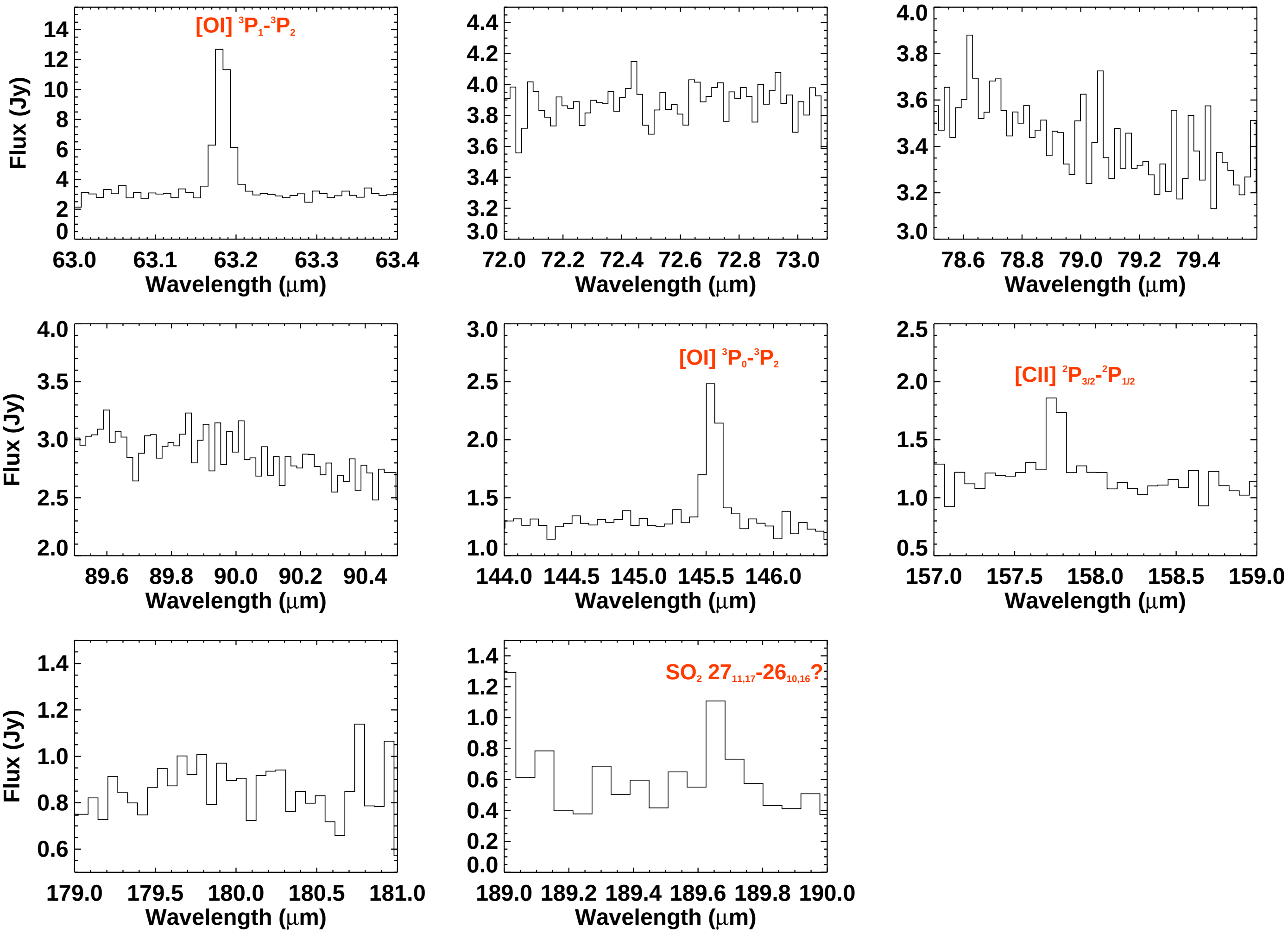

Fig. 1. Herschel spectra toward HD141569A.The peak at 189.7, which may correspond to a SO_2 line is most likely an artifact.

very well with the observed IRAS flux densities and also with the continuum flux densities measured with the PACS spectrometer (Table 2). We also observed with the PACS spectrometer to target the [O I] line at 63 μm in line scan mode, the [O I]and the [C II] lines at 145 and 158 μm, respectively in range scan mode (obsid 1342190376 PacsLineSpec and obsid 1342190375 and 1342204340 (D3) PacsRangeSpec). We reduced the spectra with the standard packages in HIPE 7.0, which include flat-field correction.

We detected the two [O I] and the [C II] lines; see Table 2. The absolute accuracy of PACS spectroscopy is currently estimated to be about 30%, but is expected to improve in the future as more calibration data are acquired and our understanding of the instrument behavior improves (see Herschel datareduction HIPE manual). Figure 1 shows the *Herschel* spectra. We may have detected an emission line at 189.67 microns, which we assign tentatively to the SO_2 $27_{11,17} - 26_{10,16}$ transition. Upper limits for transitions of CO and water are given in Table 2 and have previously been discussed in Meeus et al. (2012). The [C II] at 147 μm toward HD141569A was detected by Lorenzetti et al. (2002) using *ISO-LWS* with a flux of $3.8 \pm 0.5 \times 10^{-16}$ W m^{-2} with a beam size of $\sim 80''$, much higher than the value found by *Herschel-PACS* (11.4×10^{-18} W m^{-2}).

HD141569A was observed on 26 March 2005 with the *VLT/VISIR* instrument, the VLT Imager and Spectrometer for mid-IR (Lagage et al. 2004). The sensitivity monitored using standard stars was good (4 mJy/10σ/1h). The seeing was fair (0.7″in the optical range). The quadrangular chop-nod scheme was used to preserve the best angular resolution. The four beams were registered offline using a dedicated tool. The total on-source observing time was 533 s. We used the filter PAH1 ($\lambda_c = 8.6\,\mu m$, $\Delta\lambda = 0.42\,\mu m$), centered on the PAH emission feature. The integrated photometry is 0.532 ± 0.05 Jy. The standard star HD141569A was observed shortly before HD141569A. It was used as an estimate of the point spread function (PSF). Surface brightness profiles with and without subtracting the star were extracted along the major axis of the disk at a position angle of 0 degrees and were compared to simulated ones obtained by convolving images models with the PSF (followed by PSF subtraction). The PAH emission from HD 141569A is extended in the north-south direction (Fig. 7). Finally, we complemented the photometric points with archival data (see Table A.1) and CO ro-vibrational observations (Brittain et al. 2007), and we list in Table 2 the CO J=3–2 line flux from Dent et al. (2005).

2.2. Interstellar material toward HD141569A

Two high Galactic latitude clouds (MBM37 and the Lynds dark cloud L134N) with a hydrogen molecular fraction of 0.4 (a value of 0.5 indicates a fully molecular gas) seem to be located along the line-of-sight of HD141569A (Sahu et al. 1998). The emissions from these clouds may contaminate the disk line fluxes. Sahu et al. (1998) found a total HI column density of $N(\mathrm{H\,I}) = 8.06 \pm 0.08 \times 10^{20}$ cm^{-2} (including the two velocity components) and a H_2 column density of $N(H_2) = 1.51 \times 10^{20} \pm 9.0 \times 10^{19}$ cm^{-2} from their CH observations, whose velocity at 0 km s^{-1} is close to the CO velocities. Penprase (1992) derived a reddening $E(B-V) = 0.10 \pm 0.03$ for HD141569A.

HD141569A lies just outside the CO contour of MBM37, the molecular core associated with L134N (Caillault et al. 1995). Diffuse and molecular clouds can emit the oxygen- and carbon fine-structure emissions detected in the large pixel of PACS (9 ″ × 9″), especially the [C II] transition, which has a low critical density of 2.8×10^3 cm^{-3}, whereas the critical density for the [O I] 63 and 145 μm lines are 4.7×10^5 and 1.0×10^5 cm^{-3}, respectively (see Table 3). The critical density is the minimum gas density for the upper level of a transition to be populated in LTE. Lines are predominantly emitted in regions with a similar density or one that is higher than the critical densities.

Table 3. Molecular data of the lines.

Line	Wavelength (μm)	E_{up}/k^a (K)	n^b_{crit} (cm^{-3})	A^c (s^{-1})
OI $^3P_1 \rightarrow {}^3P_2$	63.183	227.72	4.7×10^5	8.87×10^{-5}
OI $^3P_0 \rightarrow {}^3P_1$	145.525	326	1.0×10^5	1.74×10^{-5}
CII $^2P_{3/2} \rightarrow {}^2P_{1/2}$	157.740	91.22	2.8×10^3	2.4×10^{-6}

[a] The energy of the upper state of the transition relative to the ground state in temperature.
[b] The critical density is A/γ, where A is the Einstein-A coefficient and γ the collision rate coefficient. The critical densities are computed assuming LTE, T_{kin}=100 K and the optically thin limit.
[c] Einstein-A coefficients were taken from Galavis et al. (1997).

Martin-Zaïdi et al. (2008) observed interstellar molecular hydrogen absorption lines in the UV using the *FUSE* satellite and found a column of $2.1^{+1.2}_{-0.8} \times 10^{20}$ cm^{-2}.

The total hydrogen column density of MBM37 suggests the possible contamination of the HD141569A disk emission by diffuse photodissociation region emission that fills the beam. We estimated the emission from a 1D photodissociation region (e.g., Hollenbach & Tielens 1999). According to the models of Kaufman et al. (1999), a cloud irradiated by the standard interstellar UV field (Draine field G_o=1) and with density of 10^2-10^3 cm^{-3} has a surface brightness of 10^{-8}-10^{-9} W m^{-2} sr^{-1} in [C II]. The solid angle for a pixel size of 9 ″× 9″ is 1.90×10^{-9} sr. A cloud that fills the pixel will emit $(2\text{–}20) \times 10^{-18}$ W m^{-2} in [C II], $\sim 2 \times 10^{-19}$ W m^{-2} in [O I] 63 μm, and $\sim 2 \times 10^{-20}$ W m^{-2} in [O I] 145 μm.

Alternatively, we can use the flux in the large *ISO-LWS* beam of ∼ 80″and estimate the flux in the *Herschel* beam. We found a value of 4.8×10^{-18} W m^{-2} in the *Herschel* beam assuming a uniform emitting area, a factor two lower than the observed flux. Therefore part of detected [C II] flux in the *Herschel* beam may be emitted from a foreground/background cloud.

Theoretically, cloud emission cannot account for the [O I] fluxes, but it is possible that part of the [C II] emission is emitted from the clouds associated with HD141569A or from diffuse clouds in the line-of-sight. However, if the cloud is more extended than the chop positions, any large-scale emission will be cancelled out. We also checked for extended emission from cloud or outflow emission in the 25 PACS pixels (see Fig. A.1, A.2, and A.3). Because there is no evidence for extended emission along the line-of-sight of HD141569A, we assumed that the entire [O I] fluxes arise from the circumstellar disk, while the [C II] flux may have contributions from interstellar and circumstellar material.

2.3. Simple disk analysis of Herschel line fluxes

The oxygen fine-structure line ratio 63 μm/145 μ is ∼9.8. A ratio of about 10 has been found for a large number of young stellar objects (Liseau et al. 2006). A ratio of ∼ 10 can be reproduced theoretically by optically thick emissions. Liseau et al. (2006) proposed that the 63 μm line can be re-absorbed by intervening cloud material. The two atomic oxygen and the ionized carbon fine-structure lines were detected. At first we were able to con-

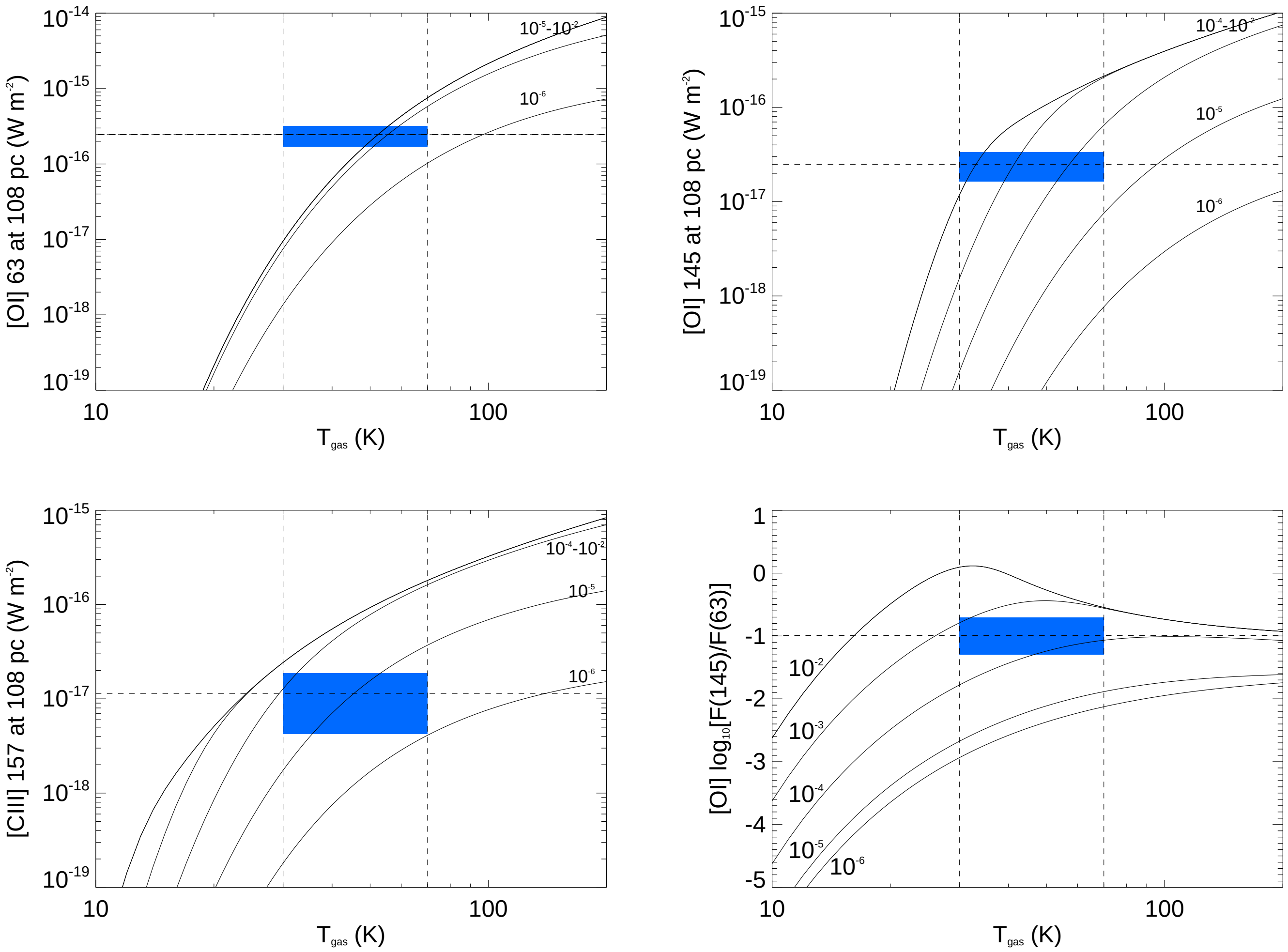

Fig. 2. Predicted [O I] 63 and 145 μm and [C II] 157 μm fine-structure fluxes as a function of the gas temperature. The fourth panel shows the predicted ratio between the [O I] 63 and 145 micron fluxes. The observed ratio is overplotted by the horizontal dashed lines. The total disk gas masses in $M_\odot$ are indicated. The blue box encompasses gas temperatures between 30 and 70 K and the observed [O I] at 63μm, [O I] at 145μm, [C II] at 157μm, and the F([O I]145μm)/F([O I]63μm) flux with 3 σ error bars.

strain the gas mass and average gas temperature from the line fluxes and their ratios. We modeled the [O I] and [C II] emissions with a simple model where the disk has a constant surface density and a radius $R_{\rm out}$. Given the disk mass and elemental abundances for atomic oxygen O and C$^+$ (Woitke et al. 2009), the vertical optical depth τ can be computed. We assumed that atomic oxygen and singly ionized carbon are the most abundant species that contain oxygen and carbon, respectively. This assumption is only valid for low-mass disks. The atomic oxygen abundance is χ(O)=8.5×10^{-4} and the ionized carbon abundance is χ(C)=3.5×10^{-4}. In an oxygen-rich environment where the gas density is low, chemical models show that atomic oxygen is by far the main carrier of oxygen. The assumed C$^+$ abundance is an upper limit to the actual value since carbon can occur in the form of atomic carbon and CO. The line fluxes in (W m^{-2}) are computed using the equation

$$\nu F_\nu \simeq B_\nu(T)(1-e^{-\tau})\frac{\pi R_{\rm out}^2}{d^2}\Delta\nu, \tag{1}$$

where $B_\nu(T)$ is the Planck function (W m^{-2} Hz^{-1}) at a single average temperature T, which is a parameter of the model, τ is the optical depth that depends on the inclination of the disk,

$$\tau({\rm O, C^+}) = \frac{c^2}{8\pi}\frac{A}{\nu^2}\left(\frac{1}{\Delta\nu}\right)\left(e^{(h\nu/kT)}-1\right)\frac{N({\rm O, C^+})}{\cos i}, \tag{2}$$

$R_{\rm out}$ is the outer radius, d is the distance ($R_{\rm out}$ and d have the same units of length), and $\Delta\nu = \nu/c\sqrt{{\rm v}_{\rm therm}^2 + {\rm v}_{\rm turb}^2}$ is the line width, with ν the frequency of the transition in Hz. N(O, C$^+$) is the oxygen or ionized carbon (C$^+$) column density.

We adopted an outer radius of 500 AU and a turbulent width v$_{\rm turb}$ of 0.15 km s^{-1}. A value of 0.3 km s^{-1} has been found in the disk around HD163296 (Hughes et al. 2011).

The values of the Einstein coefficients A and other molecular parameters are given in Table 3. The inclination is 55°. The disk mass is

$$M_{\rm gas} = \pi R_{\rm out}^2 \mu_{\rm gas}\frac{N({\rm O, C^+})}{\chi({\rm O, C^+})}, \tag{3}$$

where $\mu_{\rm gas}$= 2.2 × the atomic mass is the mean molecular mass.

We compare the line flux and line ratio predictions with the observed values and ratios in Fig. 2. We can bracket the average disk gas mass between 1×10^{-4} and 5×10^{-4} $M_\odot$ and the gas temperature between 30 and 70 K. The line optical depths as a function of the disk gas mass for a gas temperature of 60 K are shown in Fig. 4. The [O I] 63 micron emission is optically thick for disks with gas masses greater than 10^{-5} $M_\odot$, the [C II] emission becomes optically thick for gas masses greater than 10^{-4} $M_\odot$, and the [O I] 145 micron emission for gas masses greater than ~ 5×10^{-4} $M_\odot$.

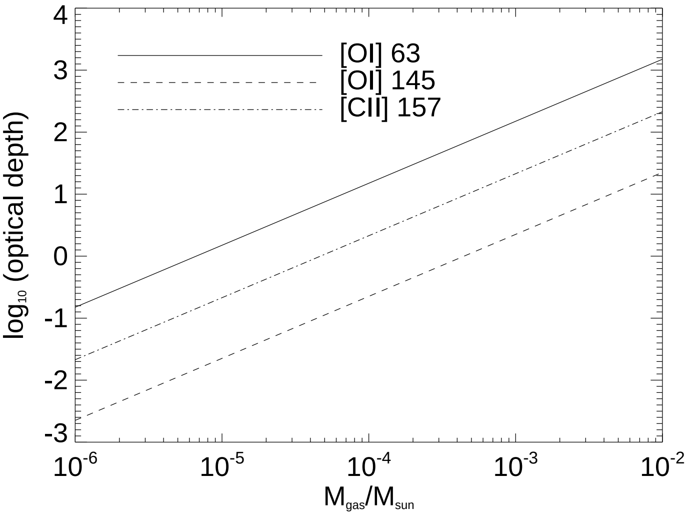

Fig. 4. [O I] 63 and 145 μm and [C II] 157 μm line optical depths as a function of the gas disk mass at $T_{\rm gas}$= 60 K.

3. Disk continuum-emission modeling

The aim of the paper is not to provide a perfect fit to the continuum data, nor to uniquely constrain the dust grain composition, but to constrain the gas- and dust (solid) disk masses. In particular, we did not attempt to fit the PAH features in detail. The continuum radiative-transfer computes the mean intensity inside the disk, which is essential for accurately characterizing the photoelectric and photoreaction processes. In addition, the fit to the SED constrains the grain surface area and temperature needed for the grain-surface interactions and adsorption/desorption processes.

3.1. Stellar properties

Accurate knowledge of the stellar properties is paramount for modeling the SED and gas lines. HD141569A is a B9.5V star with an effective temperature of 10,000 K (Merín et al. 2004) located at a distance of 99 pc (van den Ancker et al. 1997). Alternatively, Merín et al. (2004) located HD141569A at 108 pc. The stellar parameters are summarized in the upper part of Table 4.

Broad ($FWHM$ = 154 km s^{-1}) optical [O I]emission at 6300 Å centered at the stellar velocity has been detected (Acke et al. 2005) with 2.9×10^{-4} $L_\odot$, which translates into 9.5×10^{-16} W m^{-2}. In addition, the Hα emission has an equivalent width of EW=-6.7 Å. Both line profiles are double-peaked.

The star is not variable, either spectroscopically in the optical (Mendigutía et al. 2011), or photometrically in the mid-IR (Kóspál et al. 2012). Therefore it is relatively safe to use non-simultaneous photometric data. The non-variability of the star supports the idea that HD141569A is more evolved than typical HerbigAe stars.

3.2. SED modeling

3.2.1. Photometric data

We augmented the *Herschel* photometric and spectroscopic continuum data with measurements taken from the literature, which are summarized in Table A.1. These data were taken with various telescopes and beam sizes. The photometric fluxes taken with large-beam telescopes are systematically higher than the fluxes obtained with small-beam telescopes. This trend suggests a non-negligible flux contribution from foreground and background emissions. Therefore we chose to use data points from small-beam observations wherever possible.

We fitted the spectral energy distribution (SED) with the Monte Carlo continuum radiative transfer code MCFOST (Pinte et al. 2006, 2009).

The mid-IR spectrum of HD141569A is dominated by prominent PAH features with a lack of the silicate emission feature at $\lambda \simeq 10$ μm (Li & Lunine 2003; Sloan et al. 2005; Acke et al. 2010). In the absence of unambiguous constraints, we did not try to find the exact dust composition in the disk. Instead, we assumed pure amorphous magnesium-rich olivine (Mg_2SiO_4) grains (Jäger et al. 2003). We did not include carbonaceous material such as amorphous carbon or graphite, nor did we include water ice. The dust size-distribution is a power-law defined by a minimum radius $a_{\rm min}$, maximum radius $a_{\rm max}$, and power-law index p. The lack of the prominent 10-μm silicate feature hints at the presence of grains larger than a few micrometres. Furthermore to match the 1 mm flux, the maximum grain radius is probably a least a few millimeters. We adopted values for $a_{\rm max}$ between 0.5 and 1 cm. There are most likely not many solid objects larger than one centimeter in this collision-dominated disk, where the dust collision timescale is shorter than the transport timescale (Müller et al. 2010). The final values for the minimum and maximum grain radii are given in Table 4.

The dust opacity was computed according to the Mie theory for compact spherical grains and is shown in Fig. 5 for the size distribution parameters in Table 4. We used a silicate mass density of 3.5 g cm^{-3}. The extinction is dominated by dust scattering from the UV to $\lambda \simeq 10$ μm. We distinguished the dust grain mass, which includes the mass of grains up to 1 mm in radius, and the total solid mass, which corresponds to the mass of all the solids.

3.2.2. Modeling of the PAH features and image

We used circumcircumcoronene cation ($C_{150}H_{30}^+$, size~6.85 Å) as our typical PAH, because only large PAHs can survive in HerbigAe disks (Visser et al. 2007). Stein & Fahr (1985) found that large compact PAHs such as circumcircumcoronenes are extremely stable at the high temperatures (1000 K-3000 K) reached after the absorption of a UV photon. The circumcircumcoronenes can be singly negatively charged, neutral, and up to three times positively charged. In addition, the relative strengths between the PAH features in HD141569A suggest that the PAHs are large and mostly positively charged (Sloan et al. 2005; Bauschlicher et al. 2008, 2009). The PAH excitation and emission mechanisms implemented in the radiative transfer code MCFOST follow the opacity model of Draine & Li 2001, Li & Draine 2001, and Draine & Li 2007. We modeled the PAH emission profile at 8.6 μm for comparison with the observed profile.

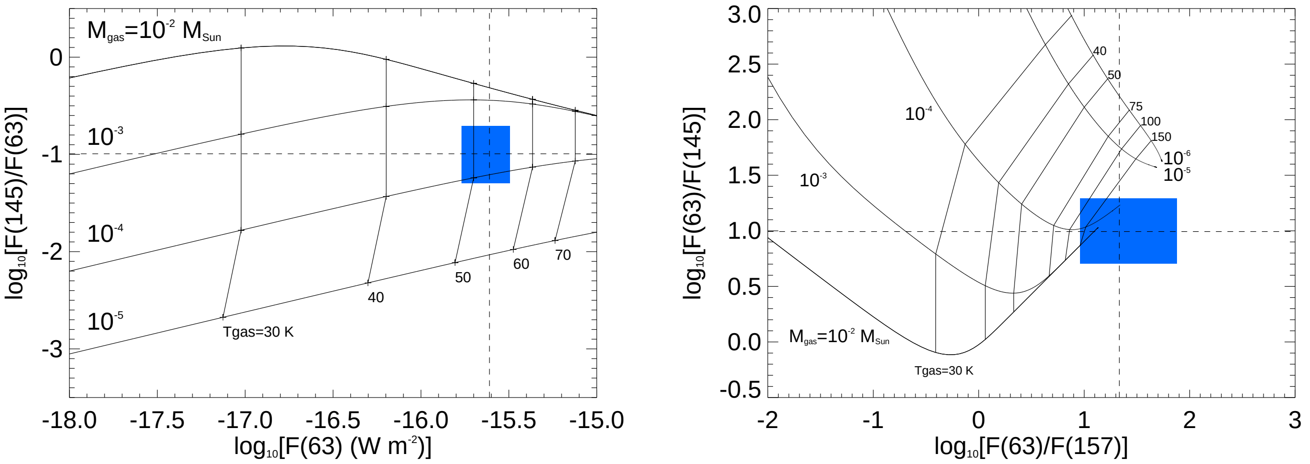

Fig. 3. Oxygen fine-structure line flux ratio as a function of [O I] 63 microns is shown in the left panel. The right panel shows the [O I] 63/[O I] 145 ratio versus the [O I] 63/[C II] 157 ratio. The blue boxes indicate the observed flux ratios. All ratios suggest a gas mass of a few 10^{-4} $M_\odot$ and a disk-averaged temperature of 75-150 K.

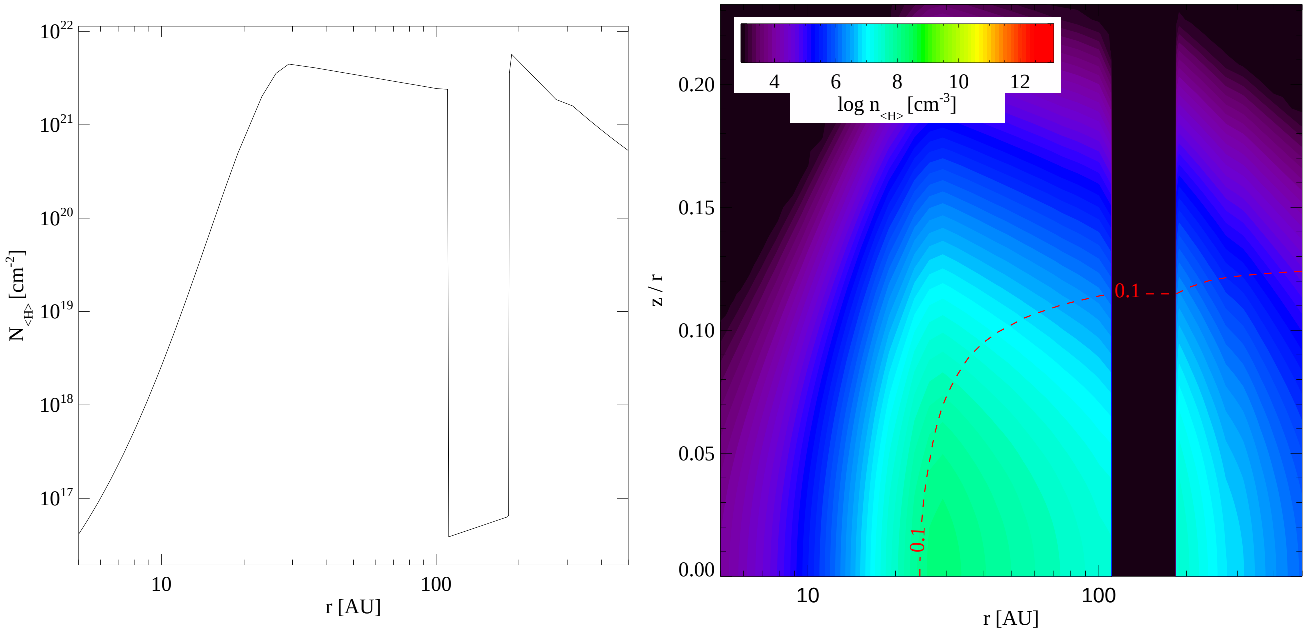

Fig. 6. Adopted half-disk surface density profile (left panel) and gas density structure for a H_0=5% opening and a gas-to-dust-mass ratio of 100 disk, ie $M_{\rm gas}$=4.9× 10^{-4} $M_\odot$ (right panel). The gap between 110 and 185 AU is not entirely devoid of gas and dust.

3.2.3. Disk structure

We adopted a parametric disk for the disk geometry. We assumed a modified version of the surface density profile of Li et al. (2003) constrained by imaging studies.

The best-fit SED is shown in Fig. 9. The disk around HD141569A is composed of three major rings peaking at ~ 15, 185, and 300 AU, respectively (see Table 4). The disk surface density and gas density structure of one of the disk models are show in Fig. 6. In that figure, the two outer rings merge into the outer disk. The location of the rings matches the scattered-light images. The disk outer radius ($R_{\rm out}$) is located at 500 AU, consistent with scattered-light images in the optical (Clampin et al. 2003). The gap between 100 and 185 AU is consistent with near-IR scattered-light and 8.6 μm images. The disk's surface geometry is defined by an opening angle H_0 at a given radius $R_{\rm ref}$ and a flaring index γ=1 (i.e., no flaring) such that the gas scale-height is given by $H = H_0(R/R_{\rm ref})^{\gamma}$. The scale-height of optically thin disks cannot be well constrained by the fit to the SED and is thus a free parameter for both the continuum and gas modeling. Therefore we ran a series of models with varying scale-height $H_0 = 3$, 5, 10, and 20 AU at the reference radius $R_{\rm ref}$= 100 AU and assumed that the gas and dust are well-mixed. The input PHOENIX stellar spectrum plotted in red is taken from Brott & Hauschildt (2005). The disk inclination i at 55° with respect to the rotation axis is well constrained by imaging data (Augereau et al. 1999). Weinberger et al. (2002) independently found an inclination of 51°. The UV spectrum of HD141569A can be entirely explained by the stellar emission without excess from gas accretion. Therefore the UV excess parameter, which accounts for non-photospheric UV emission, was set to 0.

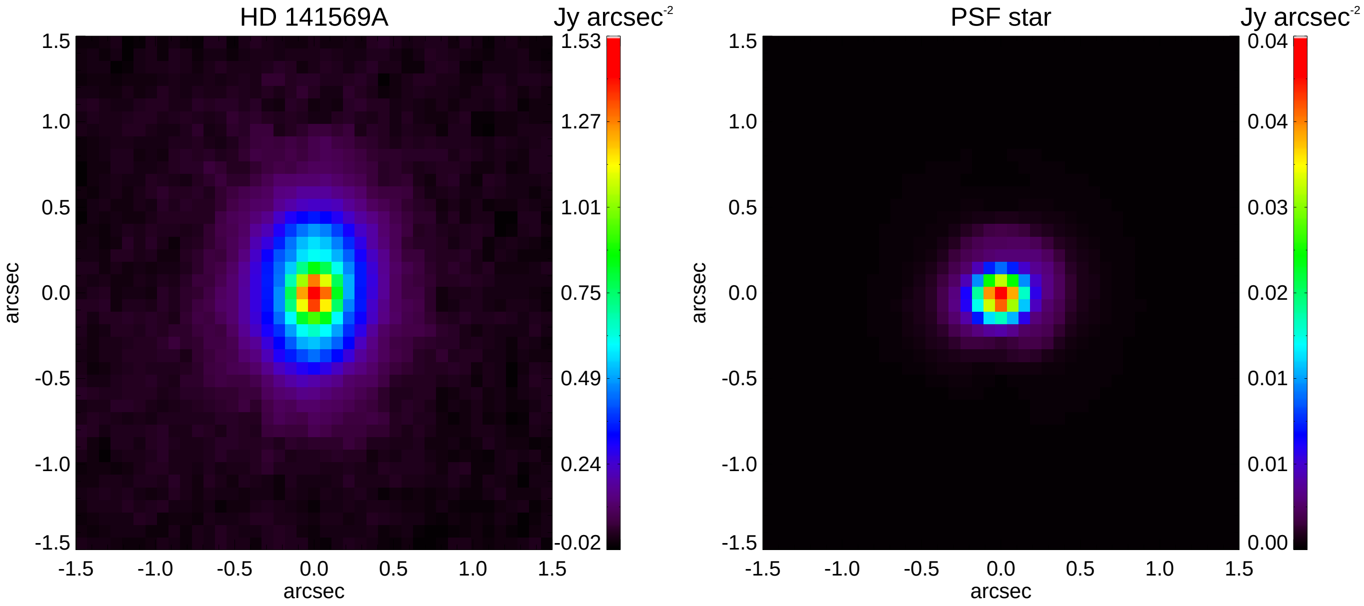

Fig. 7. Observations at the VLT with the VISIR instrument and the 8.6 microns filter (up is North, right is West). The left panel shows the image of HD 141569A and the right panel the point-spread-function star HD 146791. The disk around HD 141569A is well resolved along its major axis in the North-South direction.

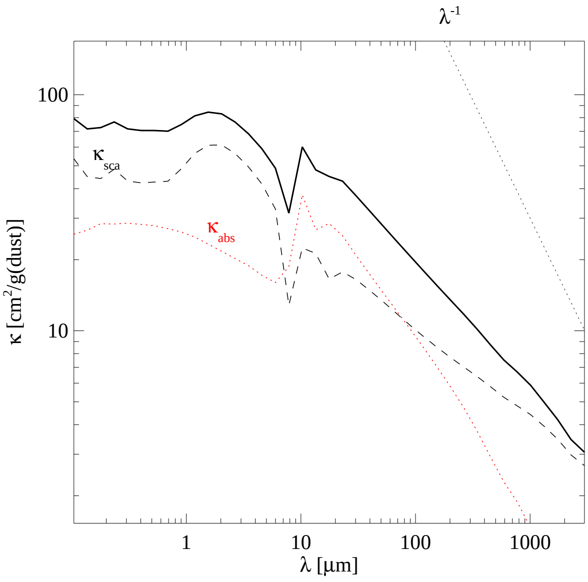

Fig. 5. Dust opacity. The dust grains are made of astronomical silicates.

The best fit to the SED is shown in Fig. 9 for the parameters listed in Table 4 and H_0 = 5 AU. The adopted surface density profile provides good fits to the SED and an 8.6 μm radial profile. The synthetic radial emission profile at 8.6 μm is compared with the radial profile observed with VISIR at the VLT (Fig. 8).

The inferred dust mass in grains with radius $\leq$ 1 mm is $M_{\rm dust} \simeq 2.1 \times 10^{-7}$ M$_\odot$ and the total mass in solids (from nanograins to pebbles) up to $a_{\rm max}$ = 1 cm is $M_{\rm solid} \simeq 4.9 \times 10^{-6}$ M$_\odot$, similar to the values found by Li & Lunine (2003) ($\simeq 6.7 \times 10^{-6}$ M$_\odot$) and Merín et al. (2004) ($\simeq 6.4 \times 10^{-6}$ M$_\odot$). The total mass of PAHs, assuming a unique size of $a_{\rm PAH}$ = 6.85 Å, is $\simeq 1.6 \times 10^{-10}$ M$_\odot$. Li & Lunine (2003) found that their best model required $M_{\rm PAH} \simeq 2.2 \times 10^{-11}$ M$_\odot$ for a PAH size distribution with a minimum radius of $a_{\rm PAH}$ = 4.6 Å. The discrepancy in the PAH mass may stem from the difference in the assumed PAH size (we used one single size whereas Li & Lunine (2003) used a size distribution for the PAHs), although we also tested the fit to the PAH features with a smaller PAH ($a_{\rm PAH}$ = 3.55 Å) and an equally good fit was obtained with the same mass of PAHs. In our modeling the PAH opacities were

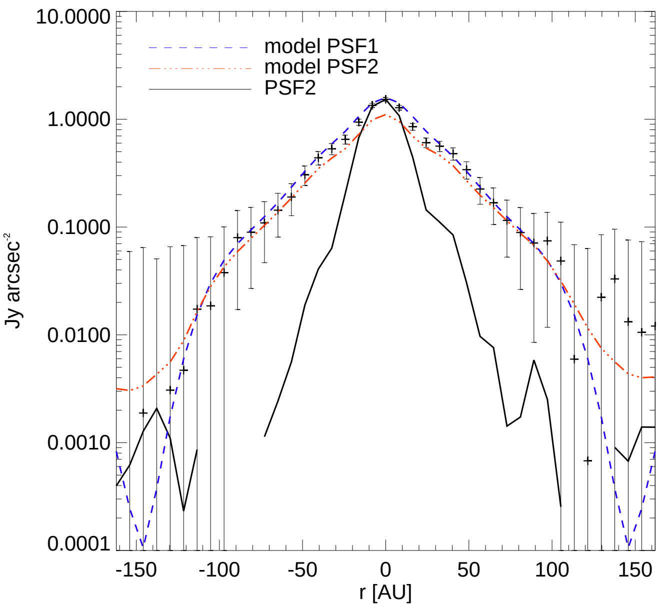

Fig. 8. Fit to the PAH radial emission profile at 8.6 μm along the major axis obtained with VISIR at the VLT. The same model has been convolved with the observed or theoretical noise-free PSF. The theoretical PSF fits the core of the observed function. The model succeeded in fitting the profile.

Table 4. Disk modeling parameters.

		Fixed parameters		
Distance	d (pc)	108		
Spectral type		B9.5V		
Stellar mass	M_* ($M_\odot$)	2.0		
Stellar luminosity	L_* ($L_\odot$)	25.77		
Effective temperature	$T_{\rm eff}$ (K)	10000		
Age	Myrs	4.71		
Solid material mass density	$\rho_{\rm dust}$ (g cm^{-3})	3.5		
ISM UV field	χ	1.0		
α viscosity parameter	α	0.0		
Non-thermal velocity	$v_{\rm turb}$ (km s^{-1})	0.15		
UV excess	$F_{\rm UV}$	0.0		
Cosmic ray flux	ζ (s^{-1})	1.7×10^{-17}		
Disk inclination	i (°)	55		
Extinction	E(B-V)	0.095		
	$R_{\rm V}$	3.1		
		Inner disk disk	Outer disk 1$^{\rm st}$ ring	Outer disk 2$^{\rm nd}$ ring
		MCFOST parameters		
Inner radius	$R_{\rm in}$ (AU)	5	185	300
Outer radius	$R_{\rm out}$ (AU)	110	500	500
Column density index	ϵ	1	3	1
Reference scale height	H_0 (AU)		3, 5, 10, 20	
Reference radius	$R_{\rm ref}$ (AU)		100	
Flaring index	γ		1	
Minimum grain size	$a_{\rm min}$ (μm)		0.5	
Maximum grain size	$a_{\rm max}$ (cm)	1	0.5	0.5
Dust size distribution index	p		3.5	
Dust mass (a ≤1 mm)	$M_{\rm dust}$ ($M_\odot$)	6.2×10^{-8}	1.8×10^{-6}	3.1×10^{-7}
Solid mass	$M_{\rm solid}$ ($M_\odot$)	2.0×10^{-7}	4.0×10^{-6}	7.0×10^{-7}
PAH mass	$M_{\rm PAH}$($M_\odot$)	2.0×10^{-11}	1.2×10^{-10}	2.1×10^{-11}
		ProDiMo parameters		
Disk gas mass	M_{gas} ($M_\odot$)	$4.9 \times 10^{-5} - 4.9 \times 10^{-4}$		

The distance and stellar parameters are taken from (Merín et al. 2004).

Table 5. PAH abundances $f_{\rm PAH}$ relative to the ISM abundance of 3×10^{-7}.

	inner disk	outer disk
$M_{\rm solid}$ ($M_\odot$)	$2.0{\times}10^{-6}$	$4.7{\times}10^{-6}$
$M_{\rm PAH}$ ($M_\odot$)	$2.0{\times}10^{-11}$	$1.4{\times}10^{-10}$
PAH	$C_{150}H_{30}$	
$a_{\rm PAH}$ (Å)	6.84	
$m_{\rm PAH}$ (a.m.u.)	1830	
$M_{\rm gas}/M_{\rm solid}$	$f_{\rm PAH}$	
100	2.0×10^{-3}	6.7×10^{-3}
50	3.9×10^{-3}	1.3×10^{-2}
20	9.9×10^{-3}	3.3×10^{-2}
10	2.0×10^{-2}	6.7×10^{-2}

taken into account, especially in the UV wavelengths, in the continuum radiative transfer, whereas Li & Lunine (2003) assumed that the disk was optically thin to the stellar radiation at all wavelengths.

The disk emission is optically thin vertically and radially from the optical to the millimeter wavelengths, thus the SED does not depend on the disk inclination. In addition, the quality of the fit to the observed photometric points does not vary strongly with the disk scale-height, as anticipated. The best fit to the SED for each gas scale-height provides the disk structure for the gas modeling with ProDiMo.

4. Gas modeling

4.1. Mass accretion rate

The mass accretion rate onto HD141569A is debated. Garcia Lopez et al. (2006) derived from the Brγ emission a current mass-accretion rate of $4{\times}10^{-9}$ $M_\odot$ yr^{-1} using an empirical relation. The derivation of the mass-accretion rate from the Brγ line is not well calibrated. It is also not known whether HD141569A

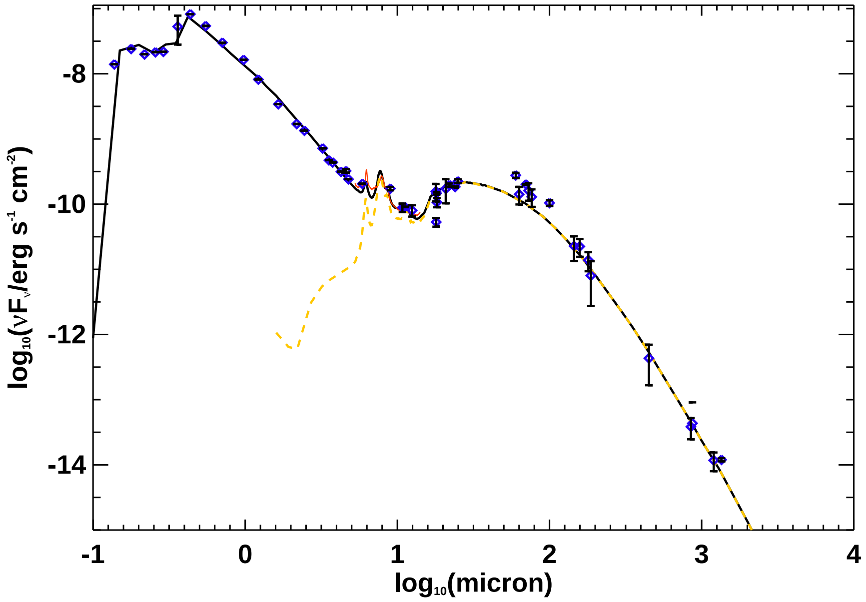

Fig. 9. Fit to the SED and the *Spitzer-IRS* spectrum by a disk model with H_0=5%. The photometric points are shown with 3σ error bars.

has a magnetosphere. The double-peaked structure observed in this fast rotator is different from to what would be expected from a line formed in a magnetosphere. On the other hand, Merín et al. (2004) did not detect mass-accretion activity and assumed a lower limit on the accretion rate of 10^{-11} $M_\odot$ yr^{-1}. Finally, Mendigutía et al. (2011) found a mass-accretion rate of 1.3×10^{-7} $M_\odot$ using the Balmer excess method. It is not clear how the accretion rate has varied during the lifetime of the disk. In the rest of the paper, we assume that the disk is passively heated.

4.2. Chemistry

ProDiMo computes the abundance at steady-state of 188 gas and ice species, including deuterated species, PAHs, and PAH ions (PAH^-, PAH, PAH^+, PAH^{2+}, PAH^{3+}). The photoreaction rates (photodissociation and photodesorption) were computed from the local UV field inside the disk and experimental or theoretical cross-sections (van Dishoeck et al. 2008). The kinetics rates were taken from the UMIST2006 database (Woodall et al. 2007) with additions and modifications. PAHs are not formed or destroyed in our chemical network and participate only in charge-exchange reactions. PAH photoionization, recombination, and charge-exchange reactions were added using the rates from Flower & Pineau des Forêts (2003).

4.3. Line emission modeling

For the line observations, we augmented the Herschel data with JCMT ^{13}CO J=3–2 observations published by Dent et al. (2005). After constraining the dust disk mass from the SED, we ran a series of models with the thermo-chemical code ProDiMo (a detailed description is given in Woitke et al. 2009; Kamp et al. 2010; Thi et al. 2011). The effects of X-rays on the gas properties in protoplanetary disks are discussed in Aresu et al. (2012, 2011) and Meijerink et al. (2012). The collisional data for the line transfer were taken from the *Leiden-Lambda* database (Schöier et al. 2005). The original references for the experimental or theoretical rates are given in Appendix A.2.

4.4. Gas kinetic temperature

The gas kinetic temperature was computed by balancing heating and cooling processes. Line profiles were computed by non-LTE radiative transfer within ProDiMo.

The disk was assumed to be passively heated with no viscous heating (α=0). Heating processes include photoelectric heating (PAHs and dust grains), fluorescence pumping followed by collisional de-excitation, gas-grain accommodation (which can also be a cooling agent), H_2 formation on grain surfaces, cosmic-ray heating, and X-ray (with a luminosity of L_X=10^{28} erg s^{-1}). For HD141569A, we assumed that the X-ray-heating is negligible compared with the heating via PAH photoelectric effects used in Meijerink et al. (2012) and Aresu et al. (2012, 2011).

The profile of the ^{12}CO J=3–2 emission line constrains the disk turbulent velocity $v_{\rm turb}$ to below 0.2 km s^{-1}. We adopted a typical value of 0.15 km s^{-1}.

The outer disk is irradiated by direct and scattered stellar photons as well as by interstellar UV photons (G_0=χ=1). The free parameters of the gas simulations are the disk gas mass $M_{\rm gas}$ (or equivalently the gas-to-dust-mass ratio since the total dust mass is fixed in the gas modeling), the fraction of PAHs in the disk with respect to the interstellar abundance $f_{\rm PAH}$, and the cosmic-ray flux ζ (=5×10^{-17} in the interstellar medium). Observations show that PAHs are depleted by at least a factor of 10 ($f_{\rm PAH}$ = 0.1) in disks with respect to the interstellar abundance in protoplanetary disks (Geers et al. 2006). We adopted the PAH abundances derived from the total PAH masses (Table 5). The gas is mostly heated by photoelectrons ejected from PAHs, whose abundance is constrained by fitting the PAH IR features. In low-mass disks irradiated by a luminous central objects, fluorescence pumping by direct or scattered stellar light can be significant. Electronic levels of OI, CII, and CO were taken into account. For CO, we included 50 rotational levels for each of the nine vibrational levels and two electronic levels (the ground- and A electronic level). The collisional rates were computed according to Thi et al. (2013).

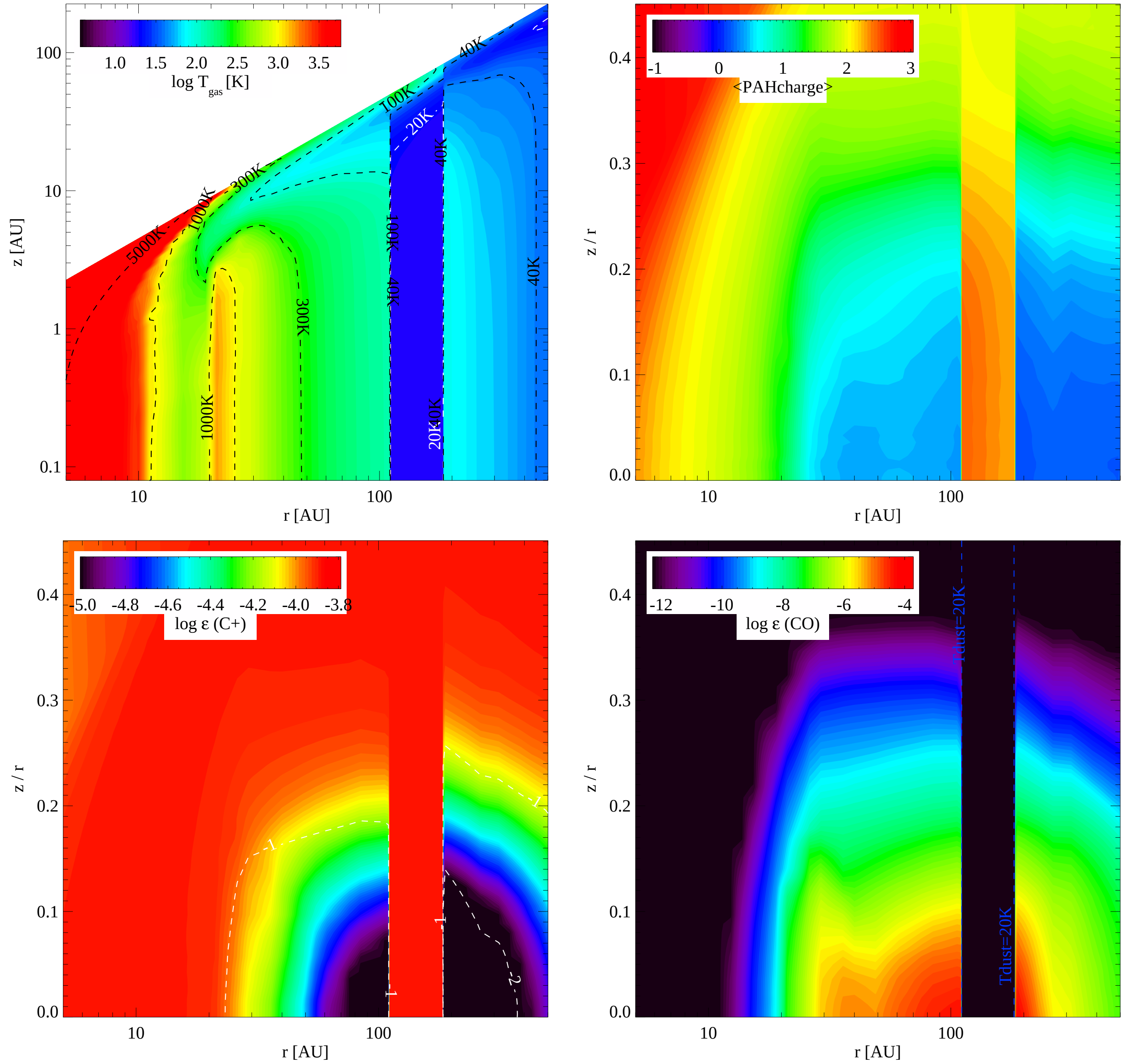

Fig. 10. The gas temperature structure (upper-left panel), PAH average charge (upper-right panel), C$^+$ abundance (lower-left panel) and the CO abundance (lower-right panel) for the model with H_0=5% and a gas-to-dust-mass ratio of 100. The gap between 100 and 185 AU is not empty but is filled with a very low density gas. The computation of the gas temperature in the low gas density gap is not reliable.

4.5. Chemistry and line modeling results

We ran a series of models for each value of the gas scale-height at 100 AU H_0: 3, 5, 10, 15, and 20 AU. In each series, the gas mass was allowed to vary such that the gas-to-dust-mass ratio was 10, 20, 50, and 100, the solid mass was kept constant. We chose to keep a constant gas-to-dust-mass ratio throughout the disk, in particular, we did not account for dust settling.

We modeled the emission of the three fine-structure lines and the CO J=3–2 line to constrain the disk gas mass. An example of the gas temperature, PAH charge, the C$^+$ and CO abundance for the disk with a 5% scale-height and a gas-to-dust ratio of 100 is shown in Fig. 10. The gas temperature shows a high-temperature feature in the 20 and 30 AU region, which corresponds to the location of the maximum surface density.

The level populations were computed at NLTE and line profiles are generated using ray-tracing. The line fluxes in W m^{-2} were obtained by integrating the line flux profiles. The locations of the fine-structure and CO J=3–2 emission are shown in Fig. 11. A summary of all model results is plotted in Fig. 12.

The gas is mostly composed of molecular hydrogen. Despite the low optical depth in both the radial and vertical direction, photodissociation of H_2 is overcome by its rapid formation on grain surfaces and self-shielding at steady-state.

Atomic oxygen is the most abundant oxygen-bearing species throughout the disk. Carbon is ionized at the disk surfaces and in the form of CO closer to the midplane (Fig.10). In the most massive disk models (M_{gas} $>10^{-3}$ $M_\odot$), CO becomes the dominant

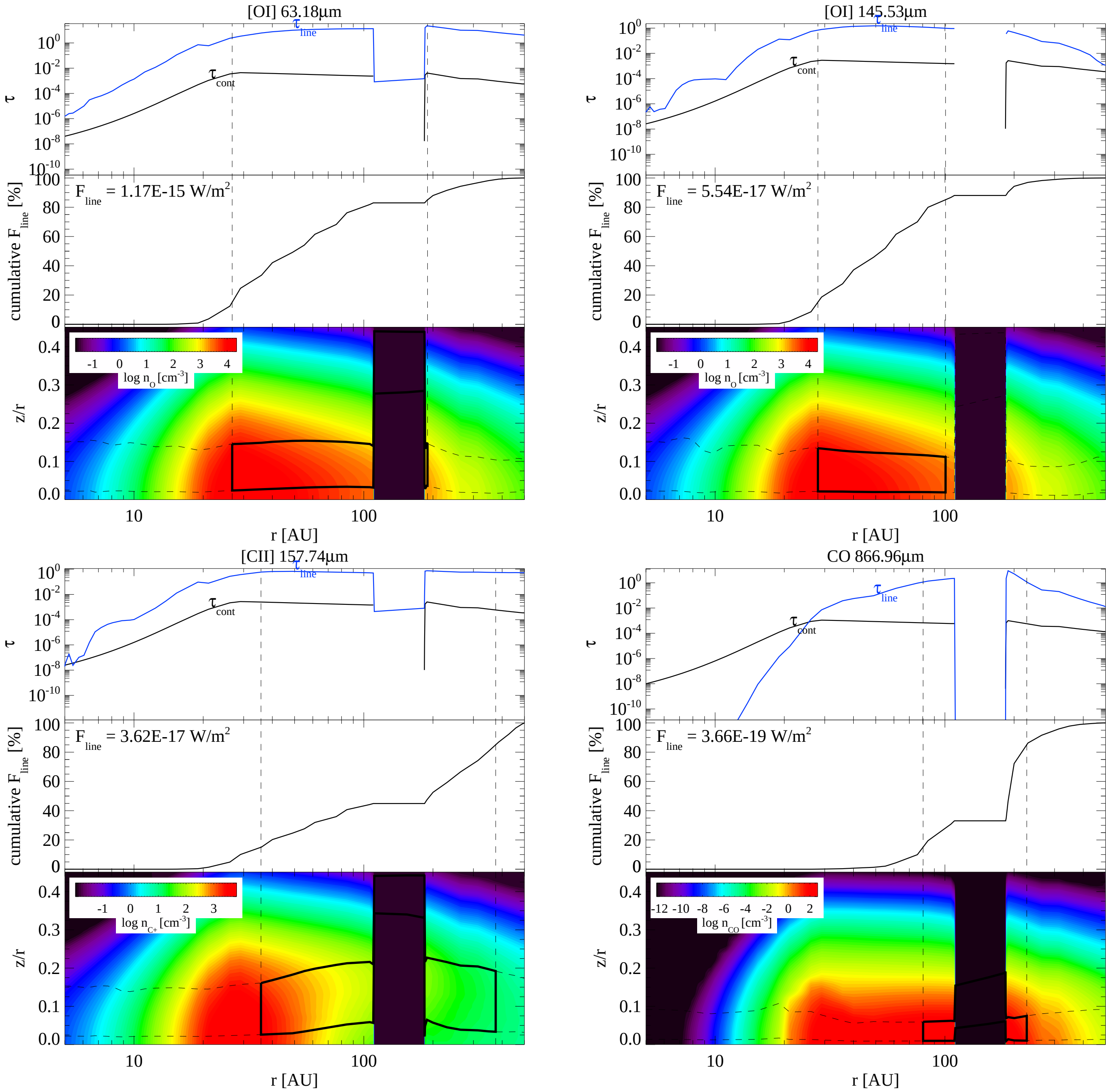

Fig. 11. The [O i] emission at 63 microns (upper-left panel), at 145 microns (upper-right panel), C ii emission at 157 microns (lower-left panel) and the CO 3-2 emission (lower-right panel) for the model with H_0=5% and a gas-to-dust-mass ratio of 100. The upper part in each panel shows the line center and continuum vertical optical depth as function of the disk radius. The middle part is the cumulative flux as function of the radius. The lower part shows the species volume density in cm^{-3}. The line fluxes are computed by ray-tracing from the opposite side of the disk toward the observer. The black boxes in the lower panels represent the regions where the vertical cumulative fluxes are at 15% to 85% of the fluxes that are emitted for half a disk. The fluxes are given for a disk seen face-on. For a given disk inclination, optical depth will change the emitted fluxes.

carbon-bearing species in the midplane (3×10^{-4} the H_2 abundance). The gas is heated by PAH photoelectrons despite the low PAH abundances compared with the interstellar abundance of ∼ 3× 10^{-7}. The PAHs are slightly positive because the electron recombination is almost as fast as the photoejection of electrons (Fig. 10). The average charge of the PAHs depends on the gas density. At low densities the photoejection rate dominates the recombination rate. CO ro-vibrational absorptions of the stellar and dust-emitted IR photons also contribute to the heating of the gas in the inner disk.

The gas is cooled by [O i] 63 μm and CO ro-vibrational line emissions, two of the main gas components of the disk in addition to H_2. The gas and the dust are not coupled thermally, which is different from more massive disks. The gas temperature in the inner disk is between 100 and 300 K, and in the outer disk it is between 40 and 100 K.

The two [O i] lines are optically thin or weakly thick for the most massive disks (Fig. 11). The [O i] lines probe the inner and outer disk. In the upper left panel of Fig. 12, all the [O i] 63 μm fluxes are higher than the observed value. The 145 μm flux varies with the gas-to-dust-mass ratio (i.e., the disk gas mass), but is not strongly dependent on the gas scale-height. The 145 μm flux can be reproduced by disk models for all gas scale-height H_0 and gas-to-dust-mass ratio of 20 to 50. The [O i] 63 μm/145 μm

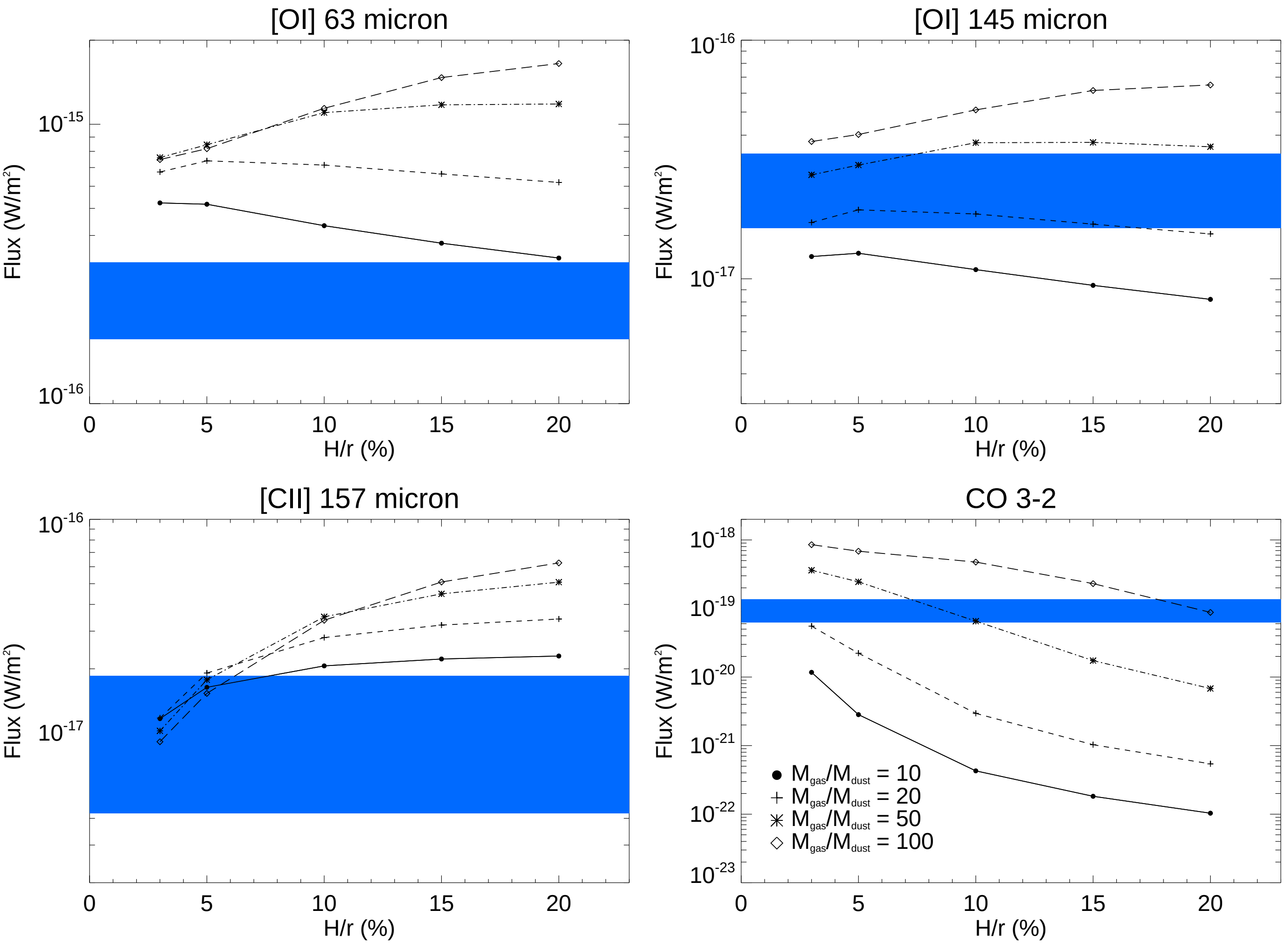

Fig. 12. Predicted [O I] 63 and 145 micron, [C II] 157 micron fine-structure and CO 3-2 fluxes as a function of the gas scale-height parameter for four different gas-to-dust-mass ratio. The observed fluxes are overplotted in blue boxes with the 3 σ error and 30% calibration error taken into account. No model fits the [O I] 63 micron line.

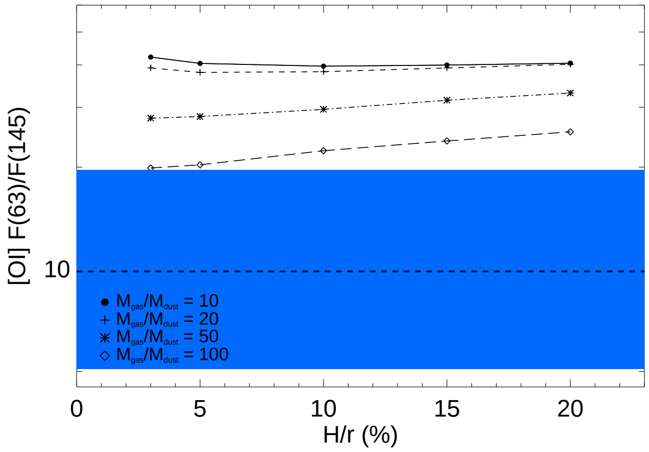

Fig. 13. [O I] 63 μm/145 μm line flux ratios as function of the disk gas scale-height for different gas-to-dust-mass ratios. The observed ratio is shown by a horizontal dash line and the uncertainties on the ratio by a blue box.

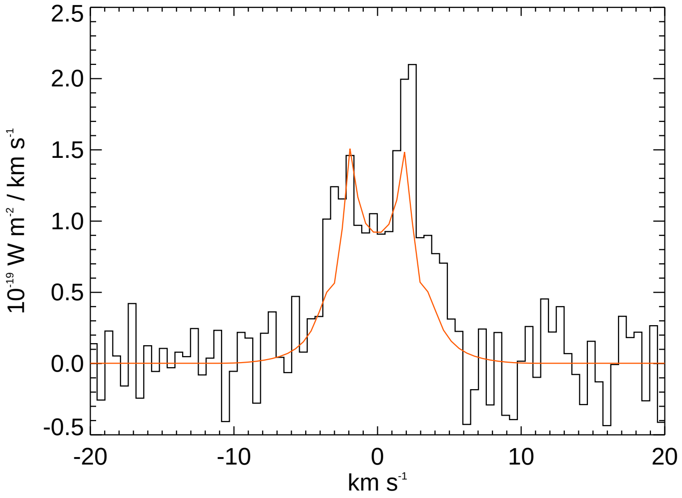

Fig. 14. Observed CO J=3–2 line profile (histogram black line) compared with the disk model-predicted profile (continuous red line). The model has an opening angle of 5% and a gas-to-dust-mass ratio of 100).

line flux ratios are shown in Fig. 13. The model ratios are higher

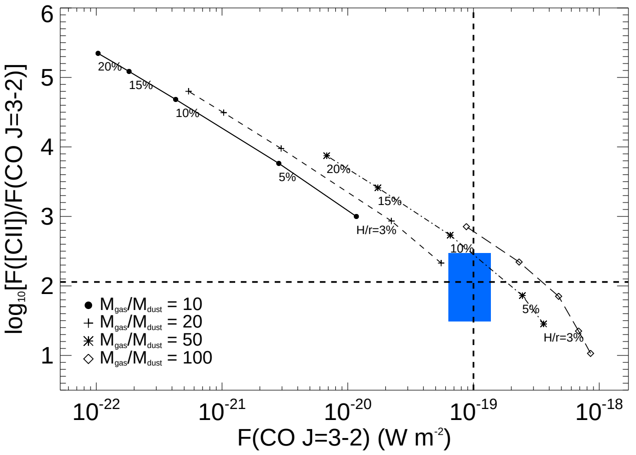

Fig. 15. Observed [C ii] / CO J=3–2 line flux ratios as a function of the CO J=3–2 line flux for different models with varying opening angles H/r (3%, 5%, 10%, 15%, and 20% as indicated on the plot) and disk gas-to-dust-mass ratios. The blue box encircles the observed ratio and flux, including the uncertainties.

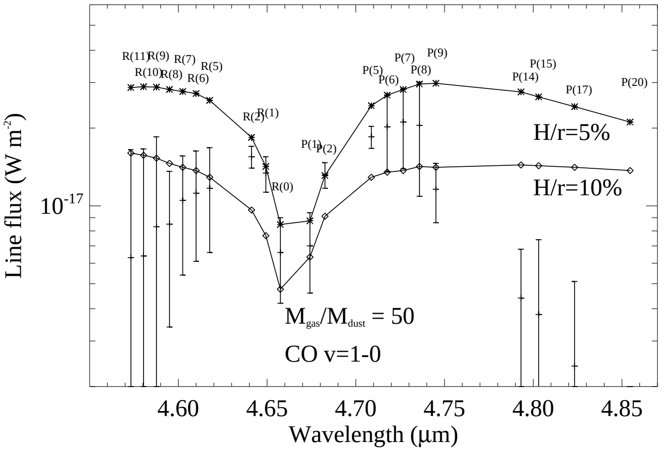

Fig. 16. Some modeled CO fundamental ro-vibrational fluxes compared with the observed fluxes taken from Brittain et al. (2007). The error bars are 3 σ uncertainties. The identification of the lines are labelled. The two models have a gas-to-dust-mass ratio of 50. The opening angles are 5% and 10%.

than 10 and decrease with increasing total disk gas mass, which reflects the effect of the line optical depth (Liseau et al. 2006).

The [C ii] line is optically thin and the flux increases with radius. [C ii] emission is emitted both by the inner and outer disk (∼ 70% by the inner disk and ∼ 30% by the outer disk, see Fig. 11). As the disk becomes more massive, more carbon is converted into CO and the disk becomes cooler. Ionized carbon is excited in gas at ∼ 100 K. The [C ii] flux first starts to increase with higher disk gas mass, but then plummets for disk gas masses greater than a few 10^{-3} $M_\odot$ (Fig. 12).

The CO J=3–2 flux increases with increasing disk gas mass. CO J=3–2 emission is generated mostly by the outer disk (70% for R > 185 AU, Fig. 11) with significant contribution from the inner disk. The CO J =3–2 flux varies dramatically with the gas scale-height for low-mass disks. Reaction rates forming CO vary as $n_{\rm H}^2$, where $n_{\rm H}$ is the gas density. In disks with large scale-heights, the gas is more diluted and the CO formation rate and self-shielding cannot compensate for the photodissociation. As a result, the [C ii] flux increases with increasing gas scale-height. An example of a predicted line profile compared with the observed spectrum obtained by Dent et al. (2005) is shown in Fig. 14. The [C ii] / CO J=3–2 line flux ratio as a function of the CO J=3–2 line flux as plotted in Fig. 15 is very sensitive to the gas-to-dust-mass ratio and gas scale-height. This plot suggests a gas-to-dust-mass ratio of ∼50 and a scale-height between 5 and 10%.

All together, the fine-structure and CO J=3–2 lines constrain the disk gas-to-dust-mass ratio between 50 to 100 and a gas scale-height of 5-10%. Especially the low value of the observed [O i] 63 μm/145 μm line flux ratio suggests a disk massive enough such that the [O i] lines become marginally optically thick.

In low-mass disks, the accuracy of CO photodissociation self-shielding factors determines the CO abundance. In all our disk models, CO is entirely in the gas-phase. The dust temperature in the outer disk is ∼40–60 K, which is higher than the sublimation temperature of CO ice. Therefore the major carbon-bearing species are ionized atomic carbon, neutral atomic carbon, and CO.

Finally, we compared the CO fundamental ro-vibrational (v=1-0) line flux predictions with the observed values of Brittain et al. (2007) in Fig. 16. We did not use the CO ro-vibrational lines to constrain the disk parameters. In general, the modeled and observed line fluxes differ within a factor two from each other for disk models with a gas-to-dust-mass ratio between 50 and 100 and a gas scale-height between 5% and 10%. The CO ro-vibrational lines are emitted between 10 AU and 50 AU consistent with the constraints given by the spatially resolved CO ro-vibrational observations of Goto et al. (2006). The CO ro-vibrational emission surface brightness is at its maximum at the location of the maximum temperature region between 20 AU and 30 AU.

In summary, the fine-structure and CO J=3–2 line fluxes suggest that HD141569A currently has a gas mass of (2.5-5) × 10^{-4} $M_\odot$. The detailed modeling suggested gas masses that are consistent with the values found by the simple interpretation in Sec. 2.3. However, the gas temperatures in the detailed models are higher than those derived from the simple analysis.

4.6. Low oxygen abundance in the disk around HD141569A?

One of the fixed parameters that was not varied is the oxygen abundance. Large amounts of oxygen can be locked as water ice onto km-sized planetesimals and decrease its gas phase abundance by a significant amount (Ciesla & Cuzzi 2006). A low oxygen abundance has been discussed as possible in the inner region of T Tauri disks (Najita et al. 2013). We tested the influence of the oxygen abundance by decreasing its value by a factor two, four, and ten in two of the models. The results are summarized in Table 6. As expected, the line fluxes of oxygen-bearing species decrease while the C ii line flux increases. However, the [O i] 63 μm/145 μm line flux ratio increases with decreasing elemental oxygen abundance as the 63 micron line becomes optically thinner. It is not clear whether a low oxygen elemental abundance can reduce the [O i] 63 micron flux without affecting the other fluxes.

5. Discussion

Line	Model 1					Model 2				
or line ratio	Observations	Std.	[O]/2	[O]/4	[O]/10 (10^{-18} W m^{-2})	Std.	self-shield.	[O]/2	[O]/4	[O]/10
[O I] $^3P_1 \rightarrow ^3P_2$	245.3 ± 4.8	1217	1100	937	640	748	569	653	556	421
[O I]$^3P_0 \rightarrow ^3P_1$	24.9 ± 1.4	67.2	40.9	24.6	12.3	37.6	28.6	19.4	11.9	7.2
[C II] $^2P_{3/2} \rightarrow ^2P_{1/2}$	11.4 ± 1.8	39.3	41.9	46.2	52.1	9.1	6.7	10.5	12.1	13.5
^{12}CO J=3–2	0.1 ± 0.008	0.79	0.49	0.27	0.08	0.85	1.46	0.68	0.47	0.18
[O I] 63/145	9.8	18.1	26.9	38.1	52.0	19.9	19.9	33.6	46.7	58.5
[C II] / ^{12}CO J=3–2	114	49.7	85.5	171.1	651.2	10.7	4.6	15.4	25.7	75

Table 6. Line fluxes from disk models: Model 1 with an opening angle of 10% and Model 2 with an opening angle of 3%. Both models have a gas-to-dust-mass ratio of 100. Four different gas-phase oxygen abundances were explore: the standard value Std, half of the standard value ([O]/2), one fourth ([O]/4), and one tenth ([O]/10).

We have explored a small grid of models varying the gas-to-dust-mass ratio and the gas vertical opening angle. None of the models manage to fit the [O I] line at 63 micron. The gas-to-dust-mass ratio is constrained by the CO J=3–2 line to be between 50 and 100. The [C II] line is sensitive to the opening angle and sets a limit of 10%. Likewise, an opening angle of 10% allows a better fit to the CO ro-vibrational lines.

5.1. A flat well-mixed disk around HD141569A

All the line fluxes suggest that the disk is flat with an opening angle smaller than 10%. It is difficult for a vertical hydrostatic disk to maintain such a flat disk for the gas. On the other hand, dust grains can decouple from the gas and settle toward the midplane, resulting in a flat dust disk. In a five-million-years old disk, most of the dust grains are expected to have settled toward the midplane. This is not clear for PAHs. A way to explain a flat gas-and-dust disk would have been that the main heating agent of the gas (PAHs) would also have settled toward the midplane. Without PAH heating, a cool gas cannot sustain itself vertically and would have collapsed toward the midplane.

5.2. Gas and dust around HD141569A

The total solid mass derived from the fit to the SED is 4.9×10^{-6} M$_\odot$, similar to the mass found by Li & Lunine (2003), even though we adopted a much simpler dust-grain composition and structure. Silicate dust grains are affected by radiative pressure (RP) and Poynting-Robertson (PR) effects. Li & Lunine (2003) estimated that $\sim 10^{-4}$ M$_\odot$ of solids have been lost either by Poynting-Robertson effect or by radiative pressure during the lifetime of the disk. At least some of the currently observed dust grains have to be replenished by collisional destruction of large planetesimals. Assuming an initial gas-to-dust-mass ratio of 100, the initial gas disk mass would have reached $\sim 10^{-2}$ M$_\odot$.

We found a total PAH mass of 1.6×10^{-10} M$_\odot$, whereas Li & Lunine (2003) found a much lower PAH mass of 2.2×10^{-11} M$_\odot$. The difference may be ascribed to the treatment of radiative transfer for the PAH excitation. The PAHs can self-shield against the UV exciting photons. The circumcircumcoronene is stable in the entire disk against photodissociation. However, PAHs are subject to RP, PR, and photodissociation. The ratio of radiative pressure to gravity is $\beta_{\rm RP} \simeq 87.4$ and is weakly size-dependent (Li & Lunine 2003). The total RP and PR PAH mass-loss rate has been estimated to reach 9.8×10^{-14} M$_\odot$ yr^{-1}. In five million years, the HD141569A disk would have lost 4.7×10^{-7} M$_\odot$ of PAHs. Assuming an initial interstellar abundance relative to hydrogen of 3×10^{-7} for the PAHs (Tielens 2008), the minimum initial gas disk mass would have been 2×10^{-3} M$_\odot$. These estimates do not take the drag between the gas and the PAHs into account. These estimates do not include PAH destruction by photodissociation, which mostly affects the small PAHs (Visser et al. 2007). Therefore the current large PAHs in the HD141569A disk are those that have been stable against photodissociation for 5 Myr.

The fine-structure and CO J=3–2 lines suggest that the HD141569A disk currently has a gas mass of (2.5-5) $\times 10^{-4}$ M$_\odot$, which translates into a gas-to-dust-mass ratio of 50–100, consistent with the interstellar value if more weight is given to the fine-structure line constraints. On the other hand, a fit to the CO J=3–2 flux alone by Dent et al. (2005) suggests a gas mass of 5×10^{-5} M$_\odot$. Jonkheid et al. (2006) modeled the outer disk around HD141569A with a gas mass of 2.4×10^{-4} M$_\odot$, compatible with our derived gas mass range.

Rotational CO lines in disks tend to require a much lower disk mass than from other gas-mass tracers (Bergin et al. 2013; Thi et al. 2001). Carbon monoxide molecules can either be photodissociated or frozen onto grain surfaces. The dust grain temperature is higher than 20 K throughout the disk such that CO freeze-out is unlikely. In addition, the disk is weakly optically thick in the UV range such that any CO molecule adsorbed onto grain surfaces will be photodesorbed almost immediately. The CO photodissociation and self-shielding processes are complicated (Visser et al. 2009). Self-shielding effects in 2D are treated approximately in the code. This simplification may result in an overestimate of the CO abundance. Once photodissociated, carbon can remain in its neutral atomic form or can be photoionized. Detections of the two [CI] fine-structure emission lines in addition to the existing CO and C II lines are necessary for determining the total gas-phase carbon budget in the disk assuming that C II, C I, and CO are the main gas-phase carbon-bearing species.

The current gas mass is 100 to 1000 times lower than the initial gas disk mass estimated from the limited lifetime of the silicate dust grains and PAHs. In five million years, a mass-loss rate via accretion or photoevaporative wind of a few 10^{-10}-10^{-9} M$_\odot$ yr^{-1} would have been sufficient for the disk to reach its current mass from an initially massive one. However, it is not clear whether a non-accreting, low X-ray emitter B9.5V star such as

HD141569A can provide enough ionizing photons to sustain a currently strong photoevaporative wind. If the dust and PAH loss-rates are correct, the HD141569A disk should have been much more massive at its formation, with an initial estimated gas mass of at least 0.01 $M_{\odot}$.

6. Conclusion

The *Herschel-PACS* spectral observations were used to constrain the dust- and gas properties surrounding the 5-Myr old HerbigAe star HD141569A. The fit to the SED and mid-IR spectrum constrains the PAH mass in the disk. The PAH abundance is depleted compared with the interstellar value ($3{\times}10^{-7}$) by a factor $2{\times}10^{-3}$ to $6.7{\times}10^{-2}$. The gas emission lines are best explained by a flat non-flaring disk. Most of the line fluxes are reproduced within a factor two except for the [O I] line at 63 μm.

We estimated the gas mass to be between 2×10^{-4} and 4.9×10^{-4} $M_{\odot}$ compared with the dust mass ($a_{\rm max}$ < 1 mm) of 2.1×10^{-6} $M_{\odot}$ or a total solid mass ($a_{\rm max}$=1 cm) of 4.9×10^{-6} $M_{\odot}$. The large uncertainty in the disk gas mass estimates comes most likely from our incomplete understanding of the physical and chemical processes that determine the chemistry in disks. Lowering the oxygen elemental abundance does not solve the problem of the very high [O I] 63 micron line fluxes in our models.

HD141569A is an example where the disk gas mass around a transitional HerbigAe star has been constrained directly from gas phase lines. However, the gas-to-dust-mass ratio depends on the gas tracer used to derive its value.

The disk solid and gas mass, as well as the disk scale-height are lower than found around other Herbig Ae stars in the *GASPS* sample, but the gas-to-dust-mass ratio remains close to the initial interstellar value of 100. If the disk around HD141569A has initially been massive ($\sim 10^{-2}$ $M_{\odot}$), the dissipation mechanisms would have removed the gas and the dust simultaneously.

Acknowledgements. We thank ANR (contracts ANR-07-BLAN-0221 and ANR-2010-JCJC-0504-01) and PNPS of CNRS/INSU, France for support. WFT, IK, and PW acknowledge funding from the EU FP7-2011 under Grant Agreement nr. 284405 (PERG06-GA-2009-256513). FM acknowledges support from the Millenium Science Initiative (Chilean Ministry of Economy), through grant "Nucleus P10-022-F". Computations presented in this paper were performed at the Service Commun de Calcul Intensif de l'Observatoire de Grenoble (SCCI) on the super-computer Fostino funded by Agence Nationale pour la Recherche under contracts ANR-07-BLAN-0221, ANR-2010-JCJC-0504-01 and ANR-2010-JCJC-0501-01. C. Eiroa, G. Meeus, and B. Montesinos are partly supported by Spanish grant AYA 2011-26202. We thank the referee for the useful comments.

References

Abrahamsson, E., Krems, R. V., & Dalgarno, A. 2007, ApJ, 654, 1171

Acke, B., Bouwman, J., Juhász, A., et al. 2010, ApJ, 718, 558

Acke, B., van den Ancker, M. E., & Dullemond, C. P. 2005, A&A, 436, 209

Andrillat, Y., Jaschek, M., & Jaschek, C. 1990, A&A, 233, 474

Aresu, G., Kamp, I., Meijerink, R., et al. 2011, A&A, 526, A163

Aresu, G., Meijerink, R., Kamp, I., et al. 2012, A&A, 547, A69

Armitage, P. J. 2010, Astrophysics of Planet Formation, ed. Cambridge University Press, Cambridge, UK

Augereau, J. C., Lagrange, A. M., Mouillet, D., & Ménard, F. 1999, A&A, 350, L51

Barber, R. J., Tennyson, J., Harris, G. J., & Tolchenov, R. N. 2006, MNRAS, 368, 1087

Bauschlicher, C. W., Peeters, E., & Allamandola, L. J. 2009, ApJ, 697, 311

Bauschlicher, Jr., C. W., Peeters, E., & Allamandola, L. J. 2008, ApJ, 678, 316

Bell, K. L., Berrington, K. A., & Thomas, M. R. J. 1998, MNRAS, 293, L83

Bergin, E. A., Cleeves, L. I., Gorti, U., et al. 2013, Nature, 493, 644

Boccaletti, A., Augereau, J., Marchis, F., & Hahn, J. 2003, ApJ, 585, 494

Brittain, S. D., Rettig, T. W., Simon, T., et al. 2003, ApJ, 588, 535

Brittain, S. D., Simon, T., Najita, J. R., & Rettig, T. W. 2007, ApJ, 659, 685

Brott, I. & Hauschildt, P. H. 2005, in ESA Special Publication, Vol. 576, The Three-Dimensional Universe with Gaia, ed. C. Turon, K. S. O'Flaherty, & M. A. C. Perryman, 565–+

Caillault, J., Magnani, L., & Fryer, C. 1995, ApJ, 441, 261

Chambaud, G., Levy, B., Millie, P., et al. 1980, Journal of Physics B Atomic Molecular Physics, 13, 4205

Ciesla, F. J. & Cuzzi, J. N. 2006, Icarus, 181, 178

Clampin, M., Krist, J. E., Ardila, D. R., et al. 2003, AJ, 126, 385

Daniel, F., Dubernet, M.-L., & Grosjean, A. 2011, A&A, 536, A76

Dent, W. R. F., Greaves, J. S., & Coulson, I. M. 2005, MNRAS, 359, 663

Dent, W. R. F., Thi, W. F., Kamp, I., et al. 2013, PASP, 125, 477

Draine, B. T. & Li, A. 2001, ApJ, 551, 807

Draine, B. T. & Li, A. 2007, ApJ, 657, 810

Dubernet, M.-L. & Grosjean, A. 2002, A&A, 390, 793

Dullemond, C. P. & Dominik, C. 2004, A&A, 417, 159

Faure, A., Crimier, N., Ceccarelli, C., et al. 2007, A&A, 472, 1029

Faure, A., Gorfinkiel, J. D., & Tennyson, J. 2004, MNRAS, 347, 323

Fisher, R. S., Telesco, C. M., Piña, R. K., Knacke, R. F., & Wyatt, M. C. 2000, ApJ, 532, L141

Flower, D. R. 2001, Journal of Physics B Atomic Molecular Physics, 34, 2731

Flower, D. R. & Launay, J. M. 1977, Journal of Physics B Atomic Molecular Physics, 10, 3673

Flower, D. R. & Pineau des Forêts, G. 2003, MNRAS, 343, 390

Galavis, M. E., Mendoza, C., & Zeippen, C. J. 1997, A&AS, 123, 159

Garcia Lopez, R., Natta, A., Testi, L., & Habart, E. 2006, A&A, 459, 837

Geers, V. C., Augereau, J., Pontoppidan, K. M., et al. 2006, A&A, 459, 545

Goto, M., Usuda, T., Dullemond, C. P., et al. 2006, ApJ, 652, 758

Hammami, K., Owono Owono, L. C., & Stäuber, P. 2009, A&A, 507, 1083

Hollenbach, D. J. & Tielens, A. G. G. M. 1999, Reviews of Modern Physics, 71, 173

Hughes, A. M., Wilner, D. J., Andrews, S. M., Qi, C., & Hogerheijde, M. R. 2011, ApJ, 727, 85

Jäger, C., Dorschner, J., Mutschke, H., Posch, T., & Henning, T. 2003, A&A, 408, 193

Jankowski, P. & Szalewicz, K. 2005, J. Chem. Phys., 123, 104301

Jaquet, R., Staemmler, V., Smith, M. D., & Flower, D. R. 1992, Journal of Physics B Atomic Molecular Physics, 25, 285

Jonkheid, B., Kamp, I., Augereau, J., & van Dishoeck, E. F. 2006, A&A, 453, 163

Kamp, I., Tilling, I., Woitke, P., Thi, W., & Hogerheijde, M. 2010, A&A, 510, A18+

Kaufman, M. J., Wolfire, M. G., Hollenbach, D. J., & Luhman, M. L. 1999, ApJ, 527, 795

Keller, L. D., Sloan, G. C., Forrest, W. J., et al. 2008, ApJ, 684, 411

Kóspál, Á., Ábrahám, P., Acosta-Pulido, J. A., et al. 2012, ApJS, 201, 11

Lacour, S., Tuthill, P., Amico, P., et al. 2011, A&A, 532, A72

Lagage, P. O., Pel, J. W., Authier, M., et al. 2004, The Messenger, 117, 12

Launay, J.-M. & Roueff, E. 1977, Journal of Physics B Atomic Molecular Physics, 10, 879

Li, A. & Draine, B. T. 2001, ApJ, 554, 778

Li, A. & Lunine, J. I. 2003, ApJ, 594, 987

Li, A., Lunine, J. I., & Bendo, G. J. 2003, ApJ, 598, L51

Lim, A. J., Rabadán, I., & Tennyson, J. 1999, MNRAS, 306, 473

Liseau, R., Justtanont, K., & Tielens, A. G. G. M. 2006, A&A, 446, 561

Lorenzetti, D., Giannini, T., Nisini, B., et al. 2002, A&A, 395, 637

Marsh, K. A., Silverstone, M. D., Becklin, E. E., et al. 2002, ApJ, 573, 425

Martin-Zaïdi, C., Deleuil, M., Le Bourlot, J., et al. 2008, A&A, 484, 225

Mathews, G. S., Dent, W. R. F., Williams, J. P., et al. 2010, A&A, 518, L127+

Meeus, G., Montesinos, B., Mendigutía, I., et al. 2012, A&A, 544, A78

Meeus, G., Pinte, C., Woitke, P., et al. 2010, A&A, 518, L124+

Meijerink, R., Aresu, G., Kamp, I., et al. 2012, A&A, 547, A68

Mendigutía, I., Calvet, N., Montesinos, B., et al. 2011, A&A, 535, A99

Merín, B., Montesinos, B., Eiroa, C., et al. 2004, A&A, 419, 301

Min, M., Dullemond, C. P., Dominik, C., de Koter, A., & Hovenier, J. W. 2009, A&A, 497, 155

Moerchen, M. M., Telesco, C. M., & Packham, C. 2010, ApJ, 723, 1418

Mouillet, D., Lagrange, A. M., Augereau, J. C., & Ménard, F. 2001, A&A, 372, L61

Müller, H. S. P. 2010, A&A, 514, L6+

Müller, S., Löhne, T., & Krivov, A. V. 2010, ApJ, 708, 1728

Najita, J. R., Carr, J. S., Pontoppidan, K. M., et al. 2013, ApJ, 766, 134

Nilsson, R., Liseau, R., Brandeker, A., et al. 2010, A&A, 518, A40

Offer, A. R., van Hemert, M. C., & van Dishoeck, E. F. 1994, J. Chem. Phys., 100, 362

Penprase, B. E. 1992, ApJS, 83, 273

Pilbratt, G. L., Riedinger, J. R., Passvogel, T., et al. 2010, A&A, 518, L1+

Pinte, C., Harries, T. J., Min, M., et al. 2009, A&A, 498, 967

Pinte, C., Ménard, F., Duchêne, G., & Bastien, P. 2006, A&A, 459, 797

Pinte, C., Woitke, P., Ménard, F., et al. 2010, A&A, 518, L126+

Poglitsch, A., Waelkens, C., Geis, N., et al. 2010, A&A, 518, L2+

Sahu, M. S., Blades, J. C., He, L., et al. 1998, ApJ, 504, 522

Salyk, C., Blake, G. A., Boogert, A. C. A., & Brown, J. M. 2011, ApJ, 743, 112

Sandell, G., Weintraub, D. A., & Hamidouche, M. 2011, ApJ, 727, 26

Schöier, F. L., van der Tak, F. F. S., van Dishoeck, E. F., & Black, J. H. 2005, A&A, 432, 369

Sloan, G. C., Keller, L. D., Forrest, W. J., et al. 2005, ApJ, 632, 956

Stein, S. E. & Fahr, A. 1985, The Journal of Physical Chemistry, 89, 3714

Sylvester, R. J., Dunkin, S. K., & Barlow, M. J. 2001, MNRAS, 327, 133

Sylvester, R. J., Skinner, C. J., Barlow, M. J., & Mannings, V. 1996, MNRAS, 279, 915

Thi, W. F., Kamp, I., Woitke, P., et al. 2013, A&A, 551, A49

Thi, W.-F., Mathews, G., Ménard, F., et al. 2010, A&A, 518, L125+

Thi, W. F., van Dishoeck, E. F., Blake, G. A., et al. 2001, ApJ, 561, 1074

Thi, W.-F., Woitke, P., & Kamp, I. 2011, MNRAS, 412, 711

Tielens, A. G. G. M. 2008, ARA&A, 46, 289

Tilling, I., Woitke, P., Meeus, G., et al. 2012, A&A, 538, A20

Turpin, F., Stoecklin, T., & Voronin, A. 2010, A&A, 511, A28+

van den Ancker, M. E., The, P. S., Tjin A Djie, H. R. E., et al. 1997, A&A, 324, L33

van Dishoeck, E. F., Jonkheid, B., & van Hemert, M. C. 2008, Fararaday Discussion of the Chemical Society, 133, 231

Visser, R., Geers, V. C., Dullemond, C. P., et al. 2007, A&A, 466, 229

Visser, R., van Dishoeck, E. F., & Black, J. H. 2009, A&A, 503, 323

Walker, H. J. & Wolstencroft, R. D. 1988, PASP, 100, 1509

Weinberger, A. J., Becklin, E. E., Schneider, G., et al. 2002, ApJ, 566, 409

Weinberger, A. J., Becklin, E. E., Schneider, G., et al. 1999, ApJ, 525, L53

Wernli, M., Valiron, P., Faure, A., et al. 2006, A&A, 446, 367

Wilson, N. J. & Bell, K. L. 2002, MNRAS, 337, 1027

Woitke, P., Kamp, I., & Thi, W. 2009, A&A, 501, 383

Woitke, P., Riaz, B., Duchêne, G., et al. 2011, A&A, 534, A44

Woodall, J., Agúndez, M., Markwick-Kemper, A. J., & Millar, T. J. 2007, A&A, 466, 1197

Wyatt, M. C. 2005, A&A, 440, 937

Yang, B., Stancil, P. C., Balakrishnan, N., & Forrey, R. C. 2006, J. Chem. Phys., 124, 104304

Appendix A: Appendix

Appendix A.1: PACS Spatial pixel emissions

Appendix A.2: Collisional data

The original articles for the line frequencies, Einstein coefficients, and collisional rates are CO (Flower 2001; Jankowski & Szalewicz 2005; Yang et al. 2006; Wernli et al. 2006), H_2O (Barber et al. 2006; Dubernet & Grosjean 2002; Faure et al. 2004, 2007; Daniel et al. 2011), O I (Abrahamsson et al. 2007; Bell et al. 1998; Chambaud et al. 1980; Jaquet et al. 1992; Launay & Roueff 1977), C II (Flower & Launay 1977; Launay & Roueff 1977; Wilson & Bell 2002), CH^+ (Müller 2010; Lim et al. 1999; Hammami et al. 2009; Turpin et al. 2010), OH (Offer et al. 1994).

Appendix A.3: Photometric data

We provide the photometric data used in our SED modeling in Table A.1.

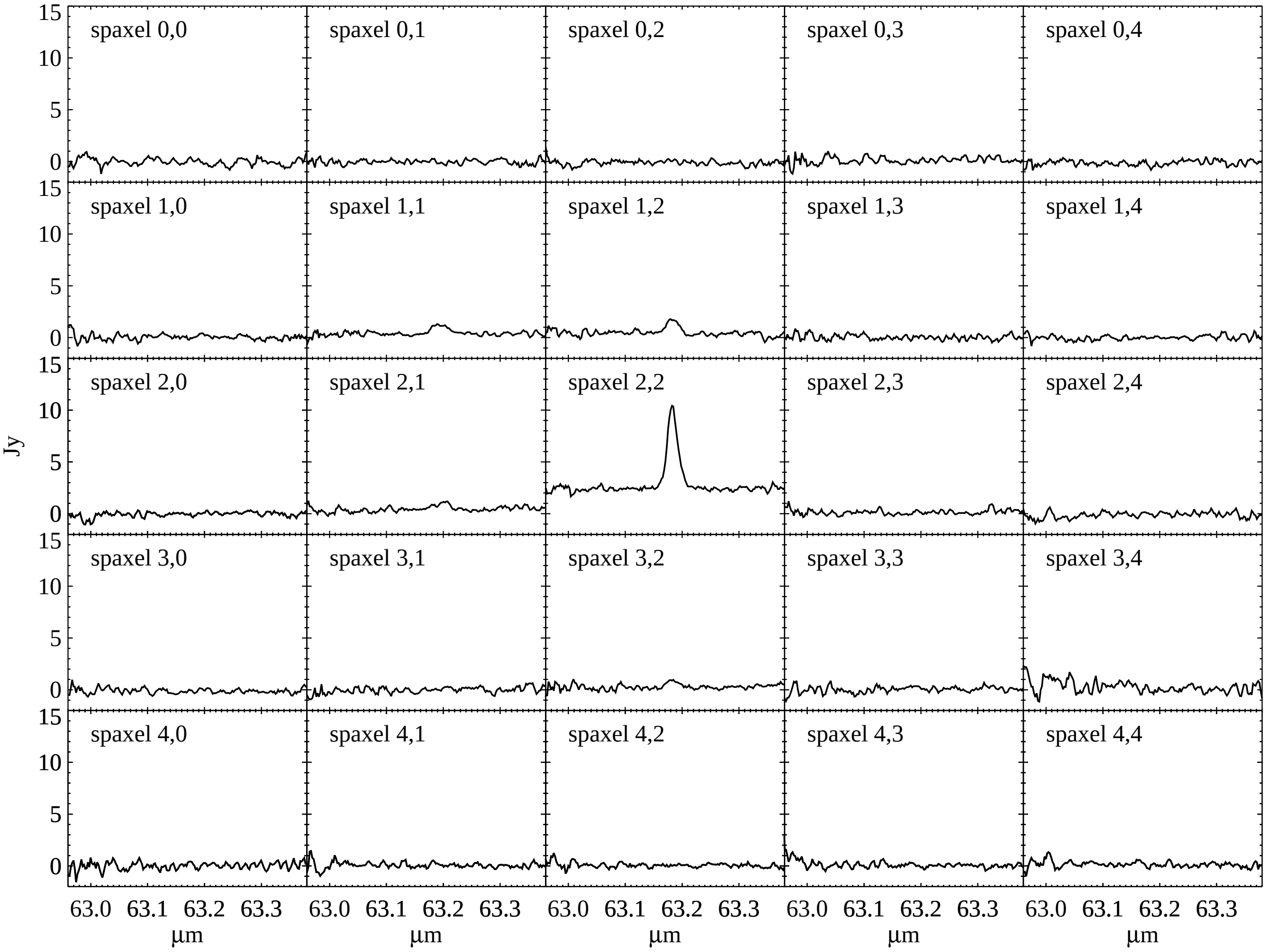

Fig. A.1. [O I] 63 μm spectrum for each pixel in the PACS spectrometer array. The PACS integral filed unit has a 47″× 47″field of view. Each 25 pixels has a 9.4″× 9.4″spatial resolution. The flux is emitted in the central spaxels.

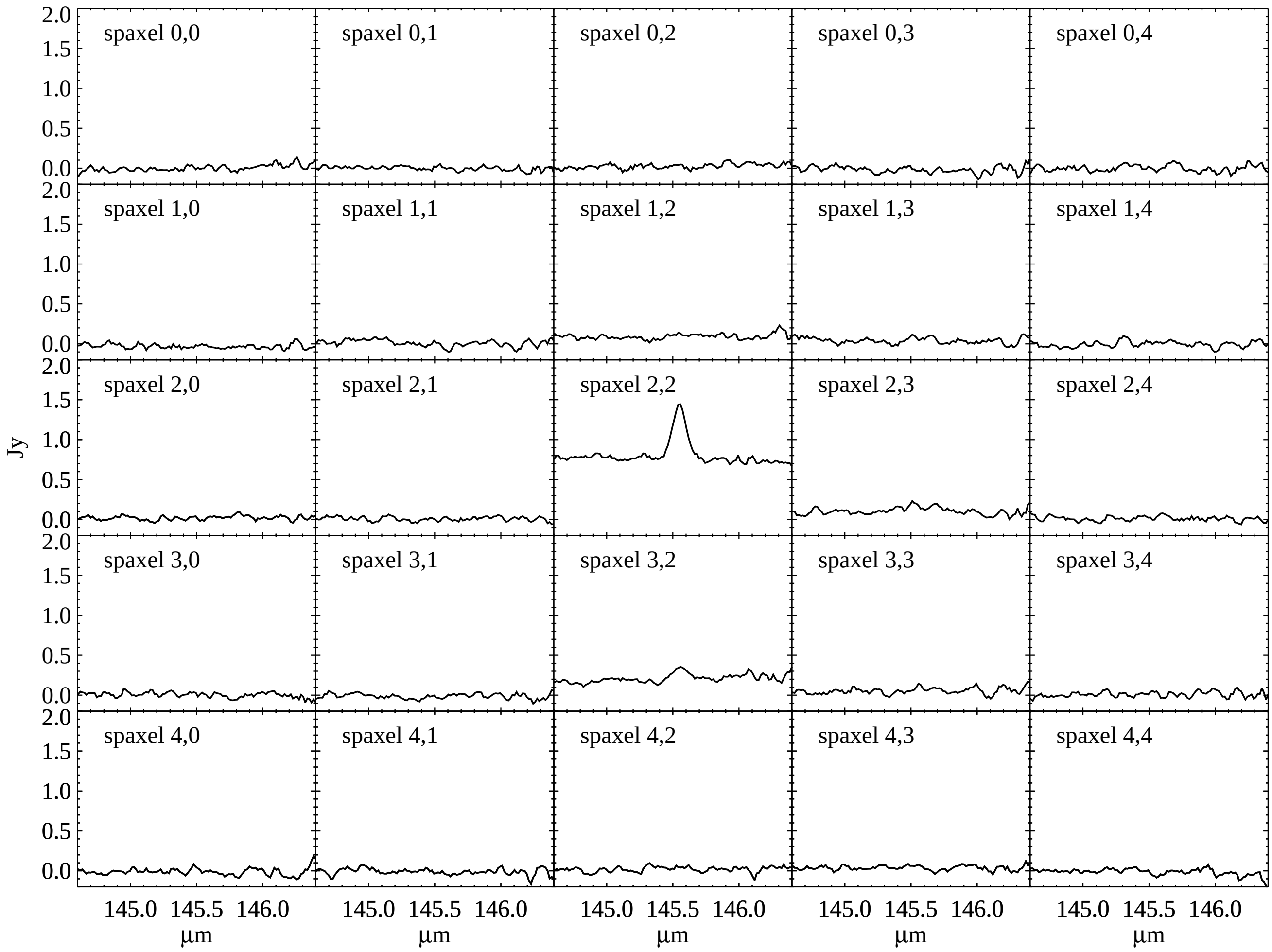

Fig. A.2. [O I] 145 μm spectrum for each pixel in the PACS spectrometer array.

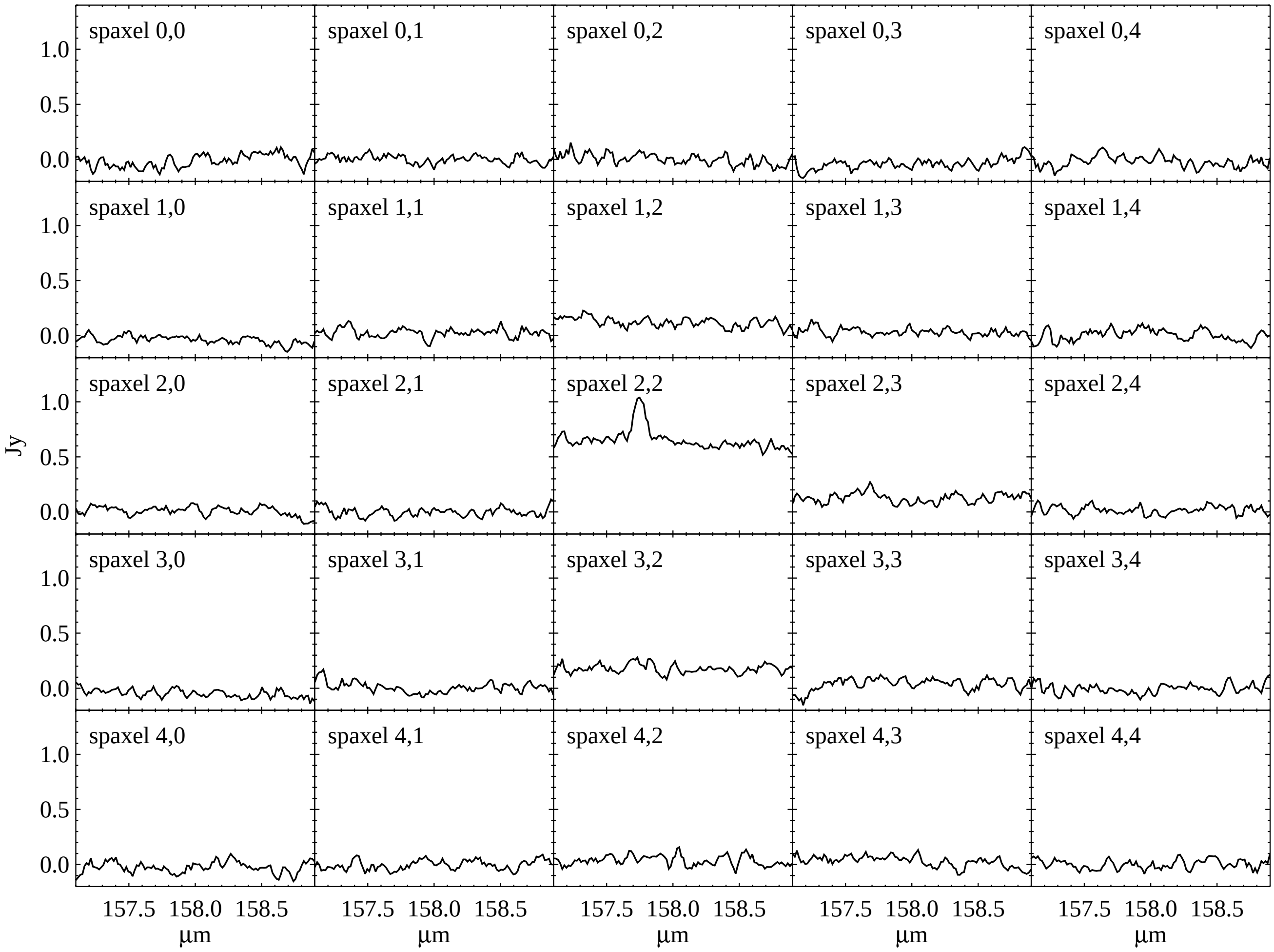

Fig. A.3. [C II] spectrum for each pixel in the PACS spectrometer array. The [C II] 157μm line is detected in the central spaxel.

Table A.1. Non-simultaneous photometric data. The data without reference are taken from Merín et al. (2004).

Band	λ (μm)	Flux (Jy)	(Beam size) and reference
IUE	0.138	0.30	archival data
IUE	0.178	0.73	archival data
IUE	0.218	0.628	archival data
IUE	0.257	1.023	archival data
IUE	0.29	1.274	archival data
U	0.36	4.19	Sylvester et al. (1996)
B	0.436	8.37	Sylvester et al. (1996)
V	0.55	7.36	Sylvester et al. (1996)
R	0.708	5.92	Sylvester et al. (1996)
I	0.977	4.81	Sylvester et al. (1996)
J	1.22	3.1	2Mass
H	1.65	1.8	2Mass
K	2.18	1.2	2Mass
ISO	2.45	1.07	ESA archive
ISO	3.23	0.76	ESA archive
WISE	3.4	0.79 ± 0.025	6.1 ″ NASA archive
UKIRT	3.76	0.54	Sylvester et al. (1996)
ISO	4.26	0.44	ESA archive
WISE	4.6	0.49 ± 0.01	6.4 ″
ISO	5.89	0.40	ESA archive
ISO	6.76	0.43	ESA archive
ISO	7.76	0.82	ESA archive
ISO	8.70	0.62	ESA archive
AKARI	9.0	0.5178 ± 0.0104	NASA archive
ISO	9.77	0.52	ESA archive
ISO	10.7	0.58	ESA archive
OSCIR	10.8	0.318 ± 0.016	Fisher et al. (2000)
Michelle	11.2	0.338 ± 0.034	Moerchen et al. (2010)
ISO	11.48	0.635	14″ × 20 ″ ESA archive
IRAS	12.0	0.55 ± 0.04	1′ × 5′ NASA archive
WISE	12.0	0.38 ± 0.006	6.5 ″ NASA archive
MIRLIN	12.5	0.333 ± 0.022	Marsh et al. (2002)
MIRLIN	17.9	0.936 ± 0.094	Marsh et al. (2002)
AKARI	18	0.8655 ± 0.0168	NASA archive
Michelle	18.1	0.883 ± 0.147	Moerchen et al. (2010)
OSCIR	18.2	0.646 ± 0.035	Fisher et al. (2000)
MIRLIN	20.8	1.19 ± 0.16	Marsh et al. (2002)
WISE	22	1.44 ± 0.027	12″ NASA archive
MIPS	24.0	1.47 ± 0.01	6 ″ Spitzer archive
IRAS	25	1.87 ± 0.13	1′ × 5′ NASA archive
IRAS	60	5.54 ± 0.49	2′ × 5′ NASA archive
PACS-Spec	63.2	2.98 ± 0.01	this paper
MIPS	70	4.70 ± 0.02	18 ″ Spitzer archive
PACS-Spec	72.8	3.91 ± 0.03	this paper
PACS-Spec	76.4	3.30 ± 0.03	this paper
PACS-Spec	90	2.80 ± 0.03	this paper
IRAS	100	3.48 ± 0.35	4′ × 5′ NASA archive
PACS-Spec	145	1.1 ± 0.1	this paper
PACS-Spec	158	1.18 ± 0.02	this paper
PACS-Spec	180	0.83 ± 0.04	this paper
SCUBA	450	0.0649 ± 0.0133	Sandell et al. (2011)
SCUBA	850	0.0140 ± 0.0020	Sandell et al. (2011)
LABOCA	870	0.0126 ± 0.0046	Nilsson et al. (2010)
MAMBO	1200	0.0047 ± 0.0005	Meeus et al. (2012)
SCUBA	1350	0.0054 ± 0.0001	Sylvester et al. (2001)